#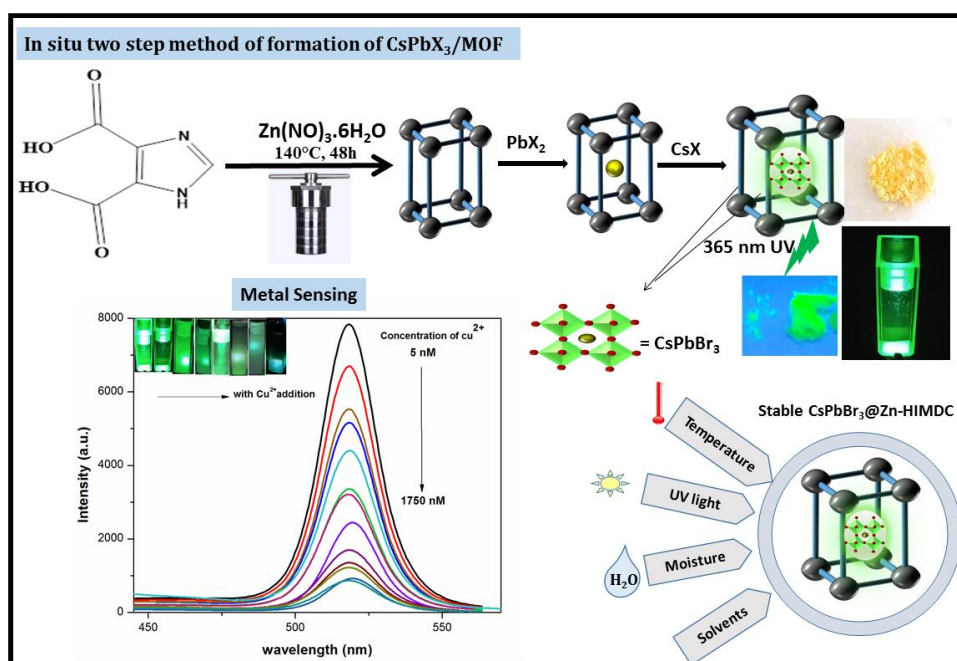 CsPbX$_3$ (X= Br, Br/Cl) perovskite quantum dots stabilized in Zinc (II) imidazole-4,5-dicarboxylate metal organic framework for metal ion detection

Highlights

This chapter deals with the synthesis of a stable CsPbX$_3$ perovskite composite using a surfactant free two step in situ growth method by introducing them into porous Zinc (II) imidazole-4,5-dicarboxylate (Zn-HIMDC) MOF for metal ion sensing application. The as prepared composite exhibits remarkable stability against moisture, ultraviolet light, heat, and polar solvents and its superior stability was explored as a luminescent probe for metal ion sensing.

This part of the thesis is published as-

Ahmed, S., Lahkar, S., Saikia, P., Mohanta, D., Das, J., and Dolui, S. K. Stable and highly luminescent CsPbX3 (X= Br, Br/Cl) perovskite quantum dot embedded into Zinc (II) imidazole-4, 5-dicarboxylate metal organic framework as a luminescent probe for metal ion detection. *Material Chemistry and Physics*, 295:127093, 2023.

2.1. Introduction

Metal halide perovskite quantum dots (PeQDs) with formula ABX_3, (A = $CH_3NH_3^+$, Cs^+, $CH(NH_2)_2^+$; B = Pb, Sn; X = Cl^-, Br^-, I^-) have attracted massive attention owing to their remarkable optoelectronic properties such as very high photoluminescence quantum yield (PLQY), narrow emission line, tunable emission wavelength, long carrier lifetime and ease of processing, etc. [1-3]. These unique properties of the aforementioned PeQDs have given them an edge over its other peers, making them a promising energy material in lighting and display technology [4], photovoltaic solar cells [5,6], photodetectors [7], sensors along with many others [8-11]. However, being a volatile organic component with a weak H-bond between the organic monovalent cation and lead halide, it degrades when exposed to extreme environmental conditions such as moisture, heat, and ultra-violet (UV) light [12,13]. These limitations of PeQDs provide one of the greatest hindrances in further exploration in research work and their mass production. To date, an optimal alternative of hybrid organic-inorganic halide perovskite PeQDs has been the use of all inorganic cesium lead halide ($CsPbX_3$) perovskite which too has arrested a lot of attention. They possess many unique optical features including ultrahigh photoluminescence quantum efficiencies, easily tunable emission colors, and absorption over the entire visible spectrum with narrow emission line widths. Protesescu et al. were the first who modified the conventional hot injection (HI) method to synthesize nanocubes of all inorganic cesium lead halide PeNCs [14]. After that, a lot of scientific attention has been applied to generate colloidal PeNCs of various sizes, shapes, and dimensions by regulating several parameters such as reaction temperature, surfactant ligand, the ratio between the surfactants and precursors, time of reaction, and B site doping with various metal ions etc. [15,16]. When compared to organic-inorganic lead halide perovskites, $CsPbX_3$ PeQDs has shown to be as efficient and stable. However, the handling of the nanocrystals (NCs) and their purification remains a daunting task. A high polar solvent dissolves the perovskite NCs, making them non-emitting, which in turn limits their practical applicability. Moreover, ion exchange reactions are caused by anion mobilities in perovskite, resulting in decomposition of the material with emission band broadening and weak PL intensity [17]. Apart from the traditional ways of synthesizing these NCs, new approaches have been developed to solve this issue.

Various stabilization techniques are used by incorporating them into robust organic polymers such as polydimethylsiloxane (PDMS), polystyrene (PS), poly

(methylmethacrylate) (PMMA), poly-(vinylidenefluoride) (PVDF), etc. or inorganic matrices e.g., amorphous silica (SiO_2), TiO_2, CaF_2, Al_2O_3 and zeolites [18–24]. Porous hybrid materials (zeolite, mesoporous silica) act as a host to encapsulate a wide variety of molecules such as quantum dots (QDs), dye, and carbon dots (CD) into their pores, as has been explored recently [25,26]. Over the past few years, research on metal-organic frameworks (MOFs), an emerging class of organic-inorganic hybrid porous materials has grabbed a lot of attention due to its wide range of advantages over other contemporary porous materials. MOFs have inorganic metal centers linked with organic linkers through coordinate bonds with intramolecular pores which enables them to possess a chain of distinct features including functional diversity, structural tunability, adjustable pore size, and very high specific surface area [27–31]. Although other materials like dye molecules, CDs, $CH_3NH_3PbBr_3$ QDs have been introduced into porous MOFs to design a range of multifunctional composites, $CsPbX_3$@MOF composite has only been reported in a few literatures, and obtaining size controlled PeQDs using such methods with potential new applications of PeQD@MOF is still a challenging process [32–37]. Since 4, 5-imidazoledicarboxylic acid (HIMDC) with its six potential donor atoms (two imidazole nitrogen and four carboxylate oxygen) and one to three removable hydrogen atoms, can act as versatile linker forming $H_{3-n}IMDC$ (n = 1, 2 or 3), making them particularly attractive as coordination ligand in metal-organic frameworks. The six donors can demonstrate a variety of coordination modes with a metal ion such as Zn^{2+} to form Zinc (II) imidazole-4,5-dicarboxylate MOF matrix (Zn-HIMDC) [38,39]. This N-heterocyclic imidazole based framework possesses permanent porosity which could enable PeQDs to incorporate into their pores. The Zn-HIMDC MOF crystal emits in the blue region, allowing energy to be transferred to the $CsPbBr_3$ perovskite QDs and increasing the flexibility of QDs emission characteristics.

In this strategy, we propose a facile two-step in situ growth of $CsPbX_3$ PeQDs into the stable Zn-based MOF (Zn-HIMDC). At first, MOF was exchanged with PbX_2 (X=Br, Cl), forming PbX_2@MOF which is then added with cesium halide. The resulting Perovskite/MOF composite made from $CsPbX_3$ and MOF is very stable under ambient conditions compared to bare $CsPbX_3$ QD, which can stay only a few hours in the ambient atmospheric condition. Compared to HI and LARP (ligand assisted reprecipitation) method for the synthesis of $CsPbX_3$ QDs, the aforementioned Zn-HIMDC MOF protected method offers a surfactant free, room temperature conversion process with very high

luminescence intensity in polar protic solvent. Using these advantages over parental $CsPbX_3$ PeQDs, we used this fluorescent composite material to detect heavy metal ions. It can be used as a photoluminescence probe for sensitive and selective detection of Cu^{2+} with a limit of detection (LOD) value of 63 nM. Their size and optical characteristics were constrained by stabilizing PeQDs on the Zn-HIMDC MOF surface. It utilizes energy transfer from the Zn-HIMDC host matrix which in turn enhances its optical properties allowing them for metal detection applications. Moreover, the existence of a dynamic quenching mechanism and electron transfer process was demonstrated through fluorescence (FL) lifetime measurement and XPS (X-ray photoelectron spectroscopy) analysis.

2.2. Experimental Section

2.2.1. Materials

Cesium bromide (CsBr, 99.9% purity, Alfa aesar[R]), lead bromide ($PbBr_2$, 99.9% purity, Alfa aesar[R]), lead chloride ($PbCl_2$ 99.9% purity, Alfa aesar[R]), oleic acid (OA, 90% purity, Alfa aesar[R]), n-octylamine (OAm, 99% purity, Alfa aesar[R]), zinc nitrate hexahydrate ($Zn(NO_3)_2.6H_2O$, 98% purity, Alfa aesar[R]), 4,5-imidazole dicarboxylic acid (HIMDC, 97% purity, Alfa aesar[R]), N,N-dimethylformamide (DMF, 99% purity, Merck[R]), toluene (C_7H_8, Merck[R]), dichloro methane (DCM, CH_2Cl_2, 98% purity, Merck[R]). All the chemicals used in this work were procured from commercial vendors and utilized without any further alteration. Ultrapure water was used for all purposes.

2.2.2. Methods

2.2.2.1. Synthesis of metal organic framework (MOF)

MOF was synthesized by following a solvothermal route in which 595 mg (2 mmol) of $Zn(NO_3)_2.6H_2O$ and 312 mg (2 mmol) of HIMDC were dissolved in 40 ml of DMF by stirring the mixture for 30 min. The resulting solution was transferred into a 100 ml teflon lined autoclave and heated at 140°C for 48 h. The solution was then allowed to cool at room temperature. The MOF crystals were obtained following several washing steps with DMF and DCM. The obtained crystals were dried under vacuum at 80°C for 2 hours for further characterization.

2.2.2.2. Preparation of CsPbBr₃ QDs without MOF

CsPbBr$_3$ QDs were synthesized following a ligand assisted re-precipitation (LARP) method where 0.2 mmol of PbBr$_2$ and CsBr were dissolved in 5 ml DMF. Then 0.5 ml of OA with 20 µl of OAm was added as capping ligand to form a clear precursor solution. 2ml of this precursor solution was then dropped into 10 ml of toluene under vigorous stirring at room temperature for one minute to nucleate CsPbBr$_3$ PeQDs. An intense green emission was detected through the mixing.

2.2.2.3. Synthesis of CsPbX₃/MOF composite

In a typical synthesis procedure of CsPbBr$_3$@MOF, the Zn-HIMDC MOF was first dispersed in 10 ml DMF. Then 2 mmol of PbBr$_2$ was added to the dispersion with continuous stirring for 5 h. The PbBr$_2$@MOF powder was collected by filtering the solution. In the second step, the resulting powder was dispersed in toluene (10 ml) with stirring. Then, the CsBr/methanol solution (1.0 mmol) was quickly injected into the toluene dispersion, which induces the crystallization of perovskite quantum dots and finally produced perovskite/MOF composite. For CsPbBr$_{3-x}$Cl$_x$@MOF preparation, DMSO was used due to the solubility difference of PbCl$_2$. The whole experiment was performed at room temperature in an ambient atmosphere. The as formed yellowish colored precipitates were collected by filtration and washed thoroughly with methanol. The synthesis method was followed from the previous literature [40].

2.2.2.4. Sensing Procedure

We used a simple protocol to evaluate how metal ion affects the luminescence intensity of CsPbBr$_3$@MOF composite in which 10 ml of the 0.1 mg ml^{-1} composite dispersion was served as the standard and thereafter emission intensity was measured. This was followed by adding calculated quantities of Cu^{2+} metal ions (in the order of 5–1750 nM) into the standard solution incubating at room temperature for 5 min. At the end of the incubation time, the PL spectra of the solutions were measured. Probe selectivity and anti-interference tests were performed for Cu^{2+} metal ion with different metal ions solution including Zn^{2+}, Bi^{2+}, Sr^{2+}, Al^{3+}, Cr^{2+}, Ca^{2+}, K$^+$, Na$^+$, Fe^{3+}, Cd^{2+}, Mn^{2+}, Co^{2+}, Ni^{2+}, Cu^{2+}, and Pb^{2+}. Along with this, Cu^{2+} and above mentioned metal ion solution were added individually to monitor the change in intensity of the test solution in the same experimental condition as above.

2.2.2.5. Fluorescence quantum yield measurement

The relative PLQY of the composite was measured using fluorescein as the reference standard (Quantum Yield = 0.95 in 0.1 M NaOH) using the equation-

$$QY = QY_S \times I/I_S \times A_S/A \times \eta^2/\eta_s^2 \qquad\qquad (2.1)$$

where,

QY = quantum yield of the sample, QY_S = quantum yield of the standard

A_S = Absorbance of the standard solution at the excitation wavelength, A = Absorbance of the composite at the excitation wavelength.

I = Integrated PL intensity of the sample, I_S = Integrated PL intensity of the standard.

η^2 = Refractive index of the solvent used for the preparation of composite solution.

η_s^2 = Refractive index of the solvent for standard.

We have prepared five different solutions of fluorescein dye and $CsPbBr_3$@MOF composite with sufficient dilution having absorbance below 0.1 and calculated the QY according to the above mentioned formula. [41]

2.2.2.6. Characterization technique

The Fourier transform infrared (FTIR) spectra and X-ray powder diffraction (PXRD) patterns were collected on a Nicolet Impact-410 IR spectrometer and D8 Focus (Bruker AXS, Germany) instrument operated at 40 kV and 40 mA using Cu Kα radiation (λ = 1.5406 Å). UV-Vis absorption spectra and photoluminescence spectra of the samples were performed at room temperature using a Shimadzu UV-2450and a Hitachi F-2700 fluorescence spectrophotometer. The relative PLQY of the composite was measured using fluorescein as the reference standard (Quantum Yield = 0.95 in 0.1 M NaOH). Time-resolved PL decay measurement was performed on a Lifespec II picosecond time-resolved fluorimeter instrument. The surface morphologies of the samples were investigated using scanning electron microscopy (SEM, Jeol JSM 6390LV) images provided with the energy dispersive X-ray spectroscopy (EDX). X-ray photoelectron spectroscopy (XPS) was carried out on the ESCALAB 220 XL spectrometer. A TECNAI G2 20 S-TWIN (200KV) was used to capture the transmission electron microscopy (TEM) and high-resolution

transmission electron microscopy (HRTEM) images of the CsPbX$_3$@MOF hybrid. The thermal behavior of the aforementioned products was deduced by using the SHIMADZU TGA-50 instrument in the presence of a constant nitrogen flow environment. A Quantachrome instrument (version 5.21) was used to obtain the N$_2$ adsorption-desorption isotherm.

2.3. Results and Discussion

2.3.1. FTIR analysis

FTIR analysis (Figure 2.1) revealed sharp peaks of ν_{asym} and ν_{sym} stretching vibrations of C=O at around 1650-1560 cm^{-1} and 1475-1380 cm^{-1} for the samples Zn-HIMDC, PbBr$_2$@Zn-HIMDC, CsPbBr$_3$@Zn-HIMDC, were ascribed to the coordinated carboxylate groups of IMDC^{2-} ligand. The Zn-O vibration was assigned a band at 663 cm^{-1}. The aforesaid findings suggested the coordination of Zn^{2+} with the IMDC^{2-} ligand. The peaks at 2921 cm^{-1} and 2852 cm^{-1} indicate the presence of OA and OAm in CsPbBr$_3$ PeQDs, assigning symmetrical and asymmetrical stretching vibration of C-H. As the synthesis method used for MOF incorporated PeQDs was a surfactant-free method, the peak at 2921 cm^{-1} and 2852 cm^{-1} were not observed for MOF incorporated PeQD. The vibrational spectrum of CsPbBr$_3$@MOF retains the characteristics vibrations of MOF implying successful passivation by the MOF matrix.
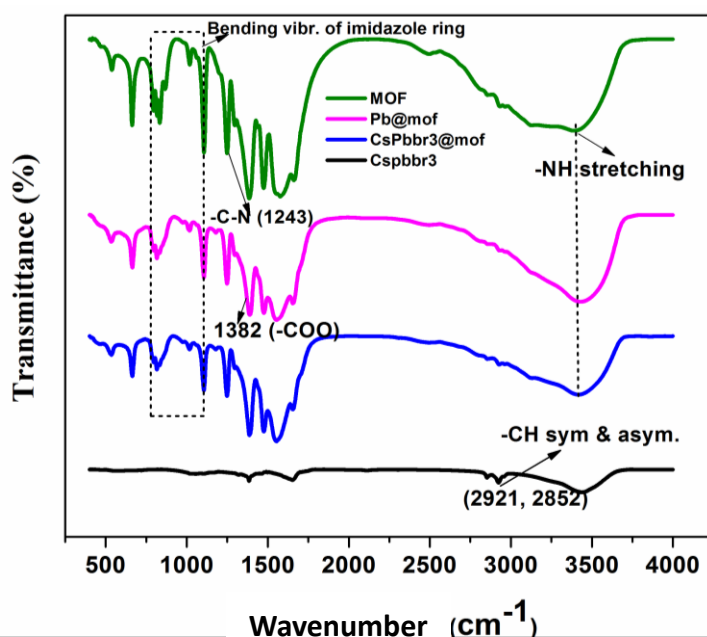

Figure 2.1: FTIR spectra of Zn-HIMDC MOF, PbBr$_2$@MOF, CsPbBr$_3$@MOF and CsPbBr$_3$ PeQDs.

2.3.2. XRD analysis

The crystal structure of the synthesized materials was studied by XRD analysis (Figure 2.2). PXRD pattern for Zn-HIMDC showed prominent peaks at $2\theta = 12.15^0$, 15.25^0, 19.6^0, 21.6^0, 26.5^0, and 30.7^0 corresponding to the (020), (200), (212), (113), and (402) characteristic planes of the MOF [39]. It indicates the phase purity and highly crystalline nature of the MOF crystal lattice. Perovskite's effective assimilation into the Zn-HIMDC matrix is shown by its similar diffraction pattern with the MOF. The relative intensities of the diffraction peak diminished and broadened after introducing $CsPbBr_3$ and $CsPbBr_{3-x}Cl_x$ into the MOF. The framework structure of MOF is preserved in all the prepared samples [32, 35]. One additional less intense peak at 43.72 (Figure 2.2b) was observed for $CsPbBr_3$@MOF corresponds to (220) plane of $CsPbBr_3$ (PDF#54-0752) [35]. The bare $CsPbBr_3$ PeQD exhibits characteristic (100), (110), (111), (200), (211), and (220) plane of $CsPbBr_3$ perovskite phase. Most of the $CsPbBr_3$ XRD peak overlapped with the MOF XRD peaks.
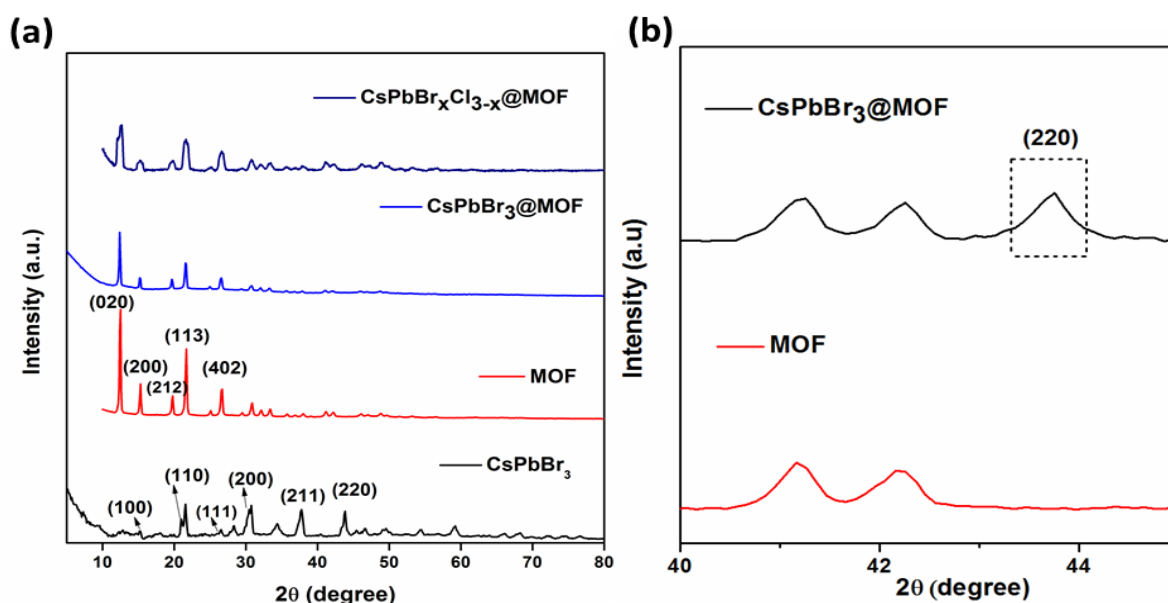

Figure 2.2: P-XRD pattern of $CsPbBr_3$, Zn-HIMDC MOF and PeQD@MOF composites (a), enlarged view of XRD pattern of $CsPbBr_3$@MOF (b).

2.3.3. Energy Dispersive X-ray Analysis (EDX)

EDX analysis (Figure 2.3) indicates the presence of component elements of MOF, bare $CsPbBr_3$ and $CsPbBr_3$@MOF composite. The C, O, N, and Zn elements are from MOF crystal and Cs, Pb, Br are from $CsPbBr_3$ PeQDs.

The presence of all C, O, N, Zn, Cs, Pb, and Br elements in the composite specifies the formation of CsPbBr$_3$@MOF composite. Corresponding elemental mapping (Figure 2.4) shows the uniform distribution of C, O, Zn, and N in the MOF and it also reveals that CsPbBr$_3$ PeQD is uniformly distributed over the entire MOF matrix.
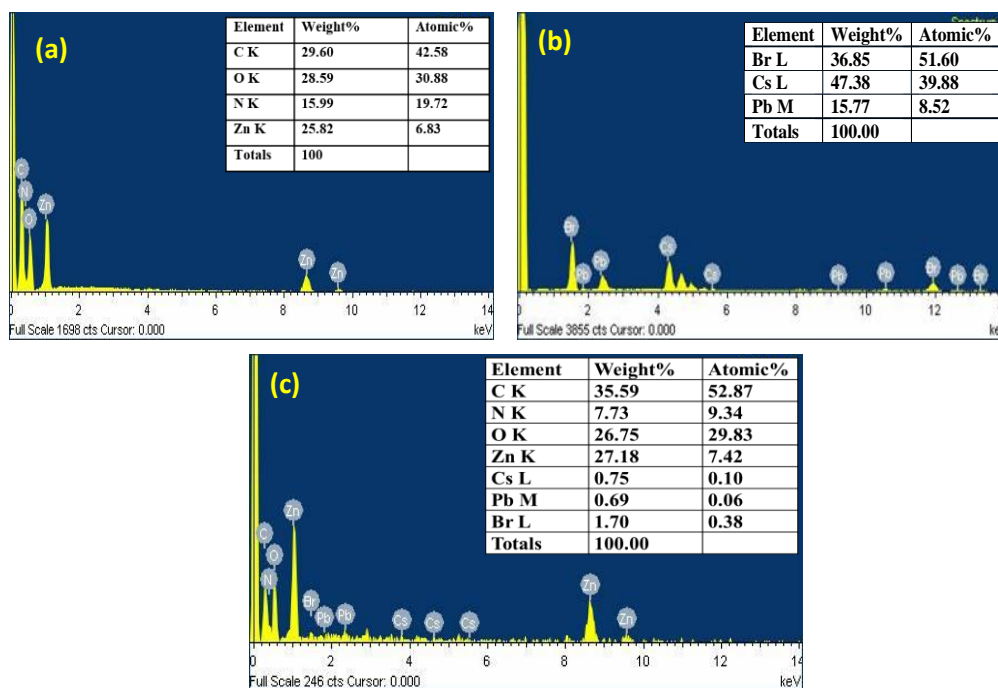

(a)

Element	Weight%	Atomic%
C K	29.60	42.58
O K	28.59	30.88
N K	15.99	19.72
Zn K	25.82	6.83
Totals	100	

(b)

Element	Weight%	Atomic%
Br L	36.85	51.60
Cs L	47.38	39.88
Pb M	15.77	8.52
Totals	100.00	

(c)

Element	Weight%	Atomic%
C K	35.59	52.87
N K	7.73	9.34
O K	26.75	29.83
Zn K	27.18	7.42
Cs L	0.75	0.10
Pb M	0.69	0.06
Br L	1.70	0.38
Totals	100.00	

Figure 2.3: EDX spectra of pristine MOF (a), CsPbBr$_3$ (b), CsPbBr$_3$@MOF (c).
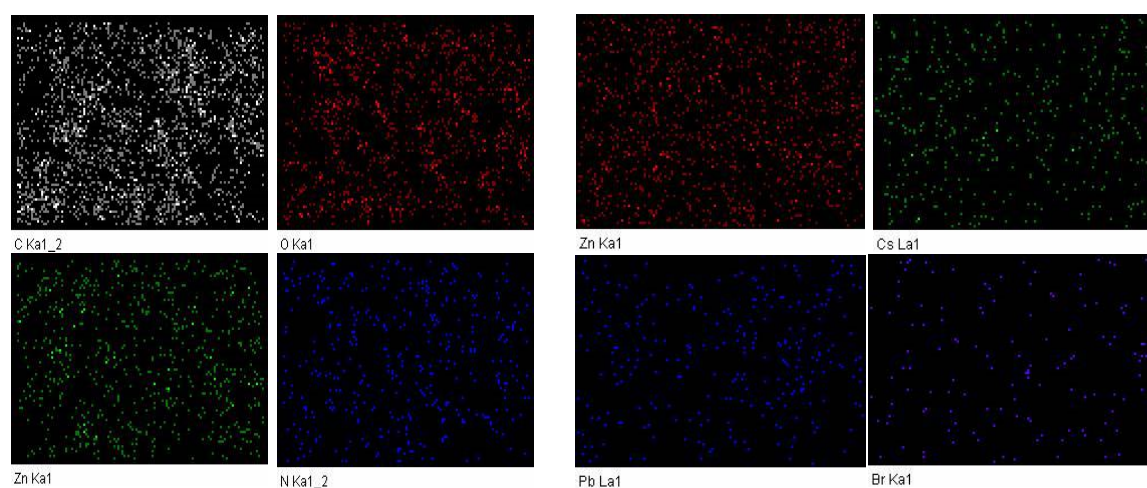

Figure 2.4: EDX Elemental mapping images of elements C, O, Zn, N of the MOF and Cs, Pb, Br, Zn of CsPbBr$_3$@MOF.

2.3.4. XPS analysis

XPS analyses were conducted to thoroughly study the surface characteristics and chemical state of the CsPbBr$_3$@MOF composite. The full XPS spectrum of the composite powder detected the signals of C, N, O, Zn, Cs, Pb, and Br elements (Figure 2.5a). The high-resolution XPS spectrum shows the features peaks of Cs $3d_{5/2}$ (723.8 eV), Cs $3d_{3/2}$ (737.7 eV), Pb $4f_{7/2}$ (138.6 eV), Pb $4f_{5/2}$ (143.4 eV), and Br $3d_{5/2}$ (67.8 eV), Br $3d_{3/2}$ (69.2 eV) of CsPbBr$_3$ PeQDs [24]. It further confirms the formation of CsPbBr$_3$ PeQDs in the MOF matrix. In addition, Zn 2p shows two peaks at 1021.2 eV (Zn $2P_{3/2}$) and 1044.2 eV (Zn $2P_{1/2}$) (Figure 2.6a). The high-resolution XPS data of C$1s$ further can be deconvoluted into three peaks at 284.2 eV (C-H/ C=C), 285.1 eV (C-N), and 288 eV (O-C=O), which are from IMDC^{2-} ligand (Figure 2.5e). The N$1s$ spectrum shows three peaks at 398.5 eV, 399.1 eV and 400.1 eV corresponding to N-Zn, N-C and N-H moieties (Figure 2.5f). It indicates the coordination of Zn^{2+} metal ion through both the oxygen and nitrogen of the linker molecule. Moreover, the O1s deconvoluted spectrum is composed of two peaks at 530.7 eV and 531.7 eV referred to (C-O-Zn) and (O=C) groups (Figure 2.6b). The XPS analysis results strongly support the formation of the CsPbBr$_3$@MOF composite.
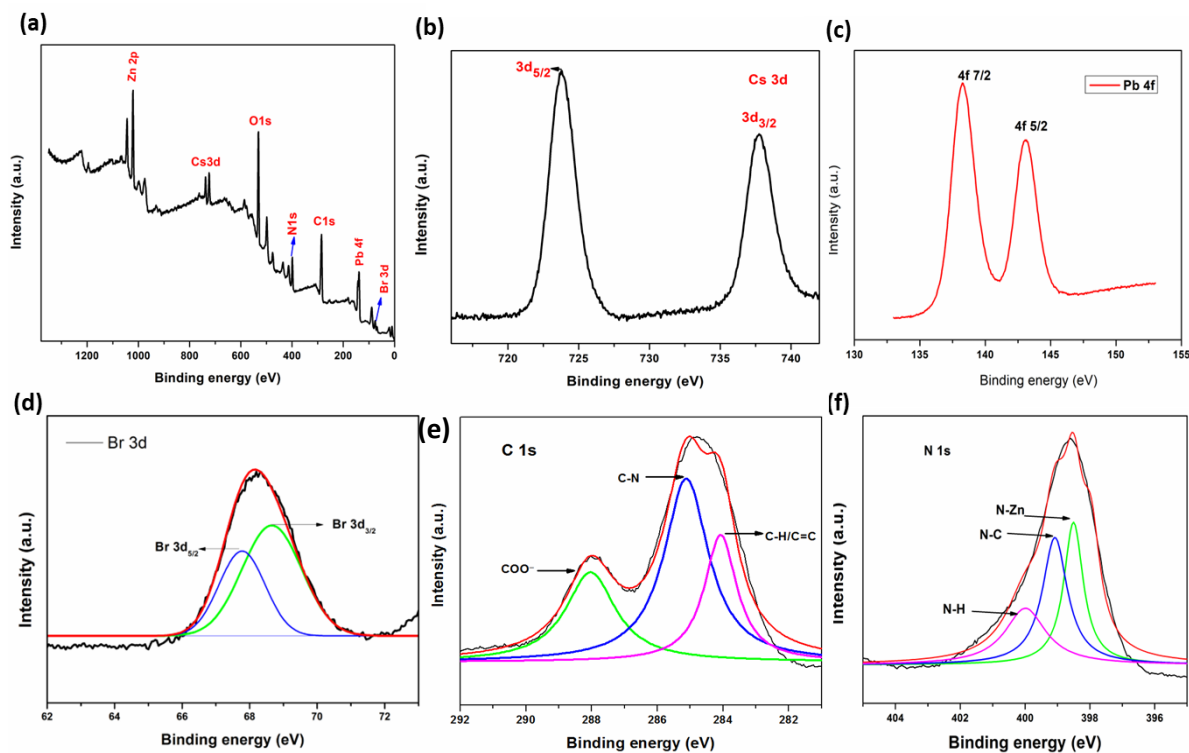

Figure 2.5: XPS full survey spectra of CsPbBr$_3$@MOF composite (a), XPS spectrum of Cs $3d$ (b), Pb $4f$ (c), Br $3d$ (d), C 1s (e), N $1s$ (f).
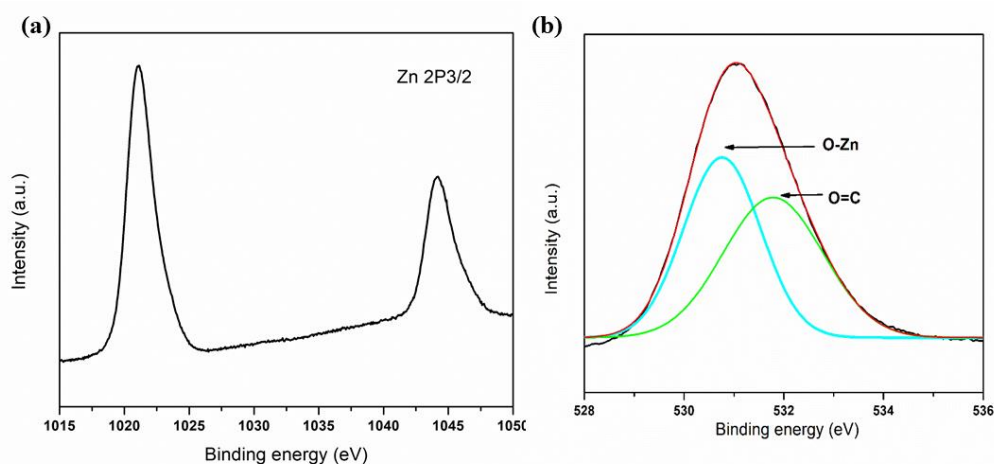
Figure 2.6: XPS fine spectra of Zn *2P* (a), O*1s* (b).

2.3.5. Morphological analysis

SEM and TEM micrograph images were taken to better understand micro-morphology and the structural evolution of CsPbBr$_3$@MOF during the two-step growth of nanocomposite material. The pristine MOF and composite are presented in Figure 2.7 as SEM images, respectively. Highly monodisperse granular shaped crystals were found for pristine MOF and measure roughly 1.5-7 micrometer in diameter with a very smooth surface. The MOF possesses a uniform and narrow size distribution with an average crystal size of about 3.8 micrometer. The morphology of MOF is preserved in the CsPbBr$_3$@MOF composite, which has the same granular shape as MOF with an average particle size of about 3.9 micrometer in length and also has uniform size distribution from 1.5-6.5 micrometer. Along with this, there were no visible nanoparticles found outside of the surface of MOF granules, which gives further indication that the majority of the particles are contained within the MOF itself. On the other hand, it is clear from Figure 2.7c, the CsPbBr$_3$ quantum dot prepared by the LARP technique without using any template possesses non uniformity in size.

Further, TEM analysis was performed to image the CsPbBr$_3$ and CsPbBr$_{3-x}$Cl$_x$ nanocrystals embedded into MOF. In the TEM image of (Figure 2.8 c) porous MOF, the pores can be seen with a disordered porous structure. The well-defined spherical PeQDs in the porous MOF matrix are clearly visible in the TEM micrography images of CsPbBr$_3$@MOF (Figure 2.8a). The average diameter of the enclosed is found to be about 3.8 nm and 3.14 nm for CsPbBr$_3$ QD and CsPbBr$_{3-x}$Cl$_x$ respectively.
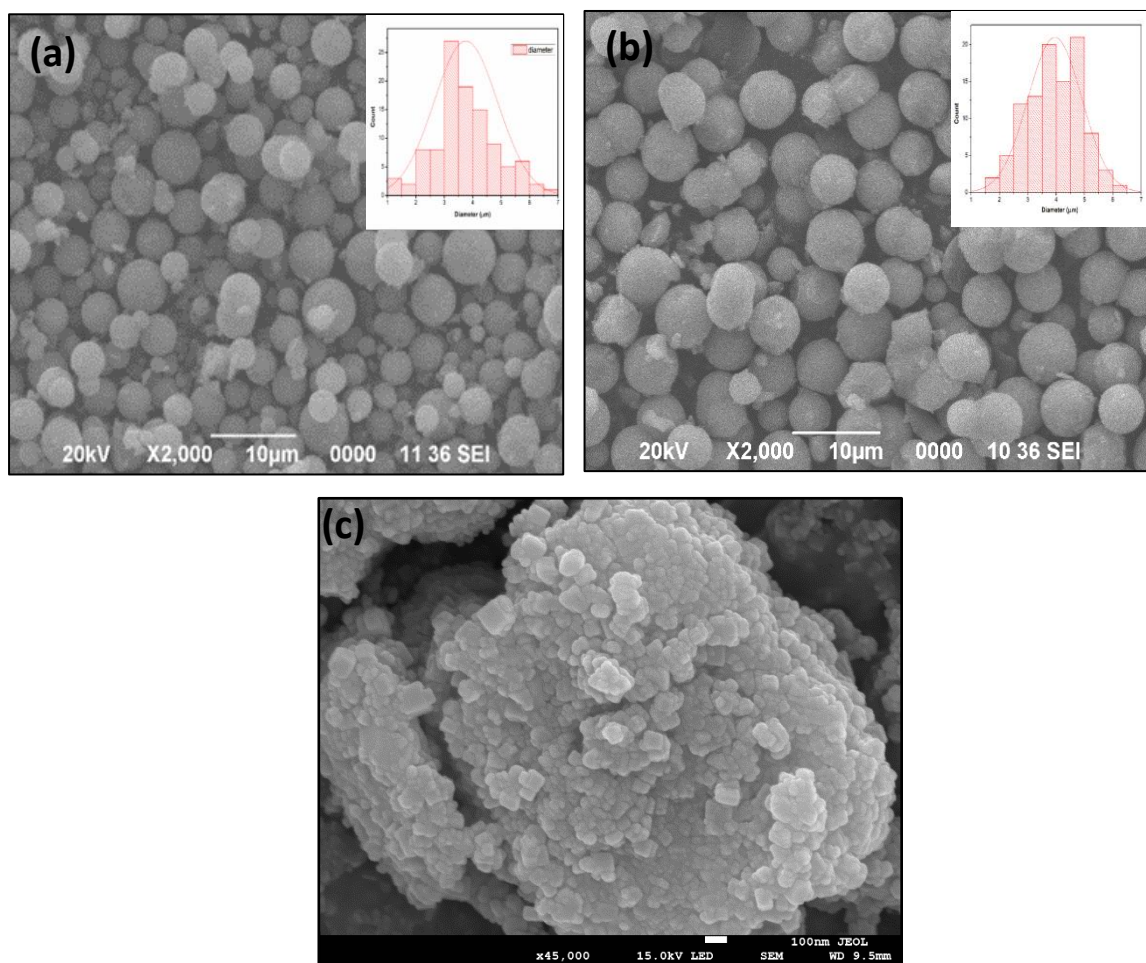
Figure 2.7: SEM images of pristine MOF (a), CsPbBr$_3$@MOF (b) with the inset shows corresponding size distribution histogram, and CsPbBr$_3$ (c).

The interplanar spacing (d- spacing) of 0.335 nm and 0.583 nm were determined from the high-resolution transmission electron microscopy (HRTEM) of CsPbBr$_3$@MOF. This corresponds to the (111) and (100) planes of the CsPbBr$_3$ respectively. In addition to this, fringe spacing of CsPbBr$_{3-x}$Cl$_x$@MOF was found to be 0.32 nm and 0.283 nm, matches well with the (111) and (200) plane of CsPbBr$_{3-x}$Cl$_x$ QD corresponding diffraction pattern at $2\theta = 27.5°$, $31.5°$ respectively [35]. As evidenced by the above findings, the CsPbX$_3$ PeQDs are shielded by the MOF matrix which would result in better stability.
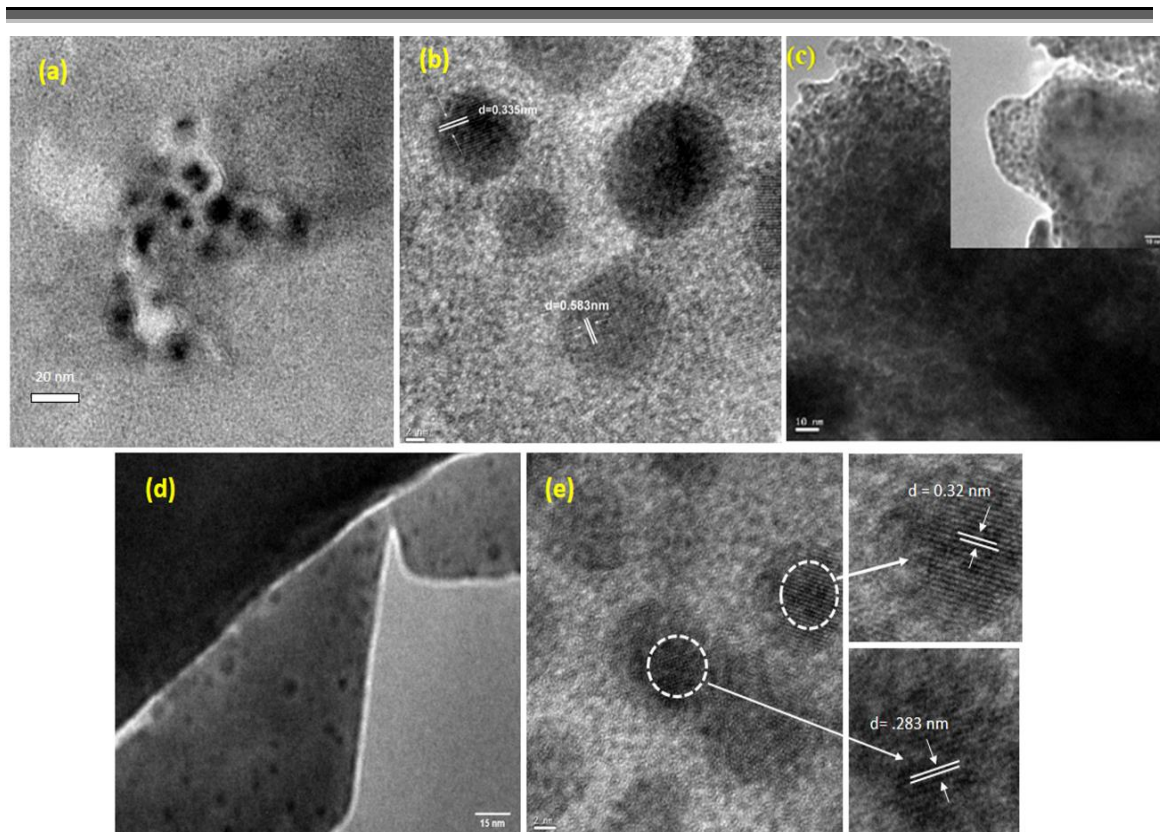
Figure 2.8: TEM images of CsPbBr$_3$@MOF composite (a, b), pristine Zn-HIMDC MOF (C) and CsPbBr3-xClx@MOF (d).

2.3.6. BET and TGA analysis

The N$_2$ adsorption-desorption isotherm at a degassing temperature of 120°C reveals that the CsPbBr$_3$@MOF composite shows a significant decrease in the overall adsorption quantity from the pristine MOF (Figure 2.9a). Pore volume (Table 2.1) was also largely decreased, indicating the growth of nonporous PeQDs and subsequent blockage of the pore channels. Thermogravimetric analysis of the Zn-HIMDC MOF and CsPbBr$_3$@MOF was carried out to study the thermal stability of these materials. TGA showed two weight loss steps (Figure 2.9b). 1st weight loss starts from around 140°C to 370°C with the maximum mass loss at about 340°C occurring from the removal of DMF linked with the metal ion. Then the 2nd weight loss from 370 to 600°C with the maximum mass loss at about 400°C indicated the decomposition of the organic linker.
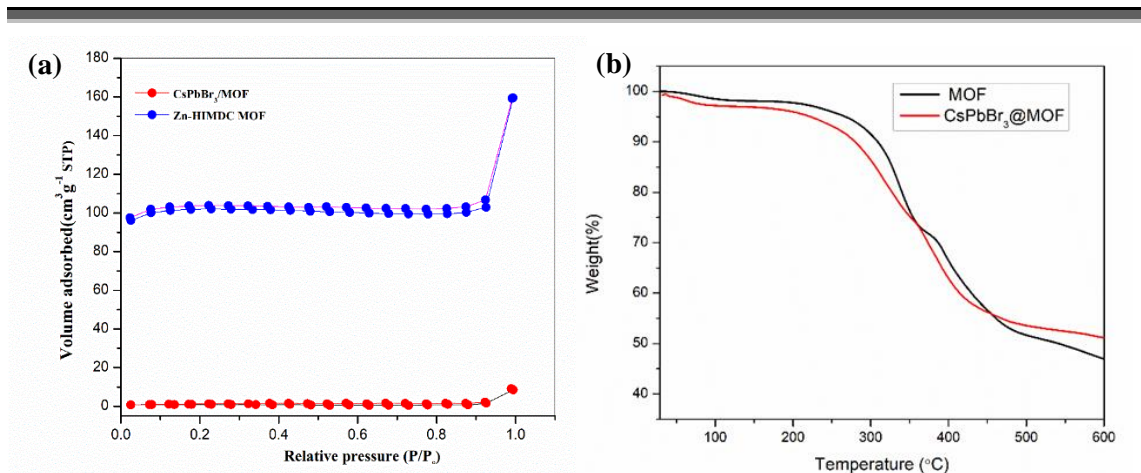
Figure 2.9: BET isotherm of Zn-HIMDC MOF and CsPbBr$_3$@MOF composite (a), TGA plot of MOF and CsPbBr$_3$@MOF composite (b).

Table 2.1. Parameters derived from BET isotherm of Zn-HIMDC MOF and CsPbBr$_3$@MOF

Sample	Pore Volume (cm^3g^{-1})	Surface area (m^2g^{-1})
Zn-HIMDC	0.096	232.511
CsPbBr$_3$@MOF	0.015	3.18

2.3.7. Optical properties of MOF, PeQD@MOF

The Zn-HIMDC MOF exhibited a broad blue emission on excitation at 365 nm wavelength with a maxima located at 446 nm with the full-width half maxima (FWHM) of 123 nm (Figure 2.10a). This emission peak of MOF is mostly caused by free HIMDC linker emission which has a weak emission peak at about 438 nm under 365 nm excitation and FWHM at 95.58 nm, possibly due to intra ligand $\pi \rightarrow \pi^*$ transition [30,42]. The emission peak of the MOF had a red shift of 8 nm and a considerable luminescence amplification as compared to the free linker (L). It indicates the interaction of Zn^{2+} metal ions with the (HIMDC)$^{2-}$ (LMCT transitions) in a variety of ways [30,39]. When excited under 365 nm wavelength. CsPbBr$_3$@MOF exhibits dual emission (Figure 2.10b). A broad emission peak located at 434 nm and a sharp narrow green emission peak at 519 nm with FWHM of 20.52 nm was observed in the emission spectra of the aforementioned CsPbBr$_3$@MOF composite. The very narrow FWHM value indicates the homogeneity of the composite in terms of size and defects along with the high color purity of the generated green color. The

first peak that appeared at 434 nm could be due to Zn-HIMDC MOF and the sharp green emission peak assigned to the emission of $CsPbBr_3$ PeQDs. The $CsPbBr_3$@MOF composite has a relative quantum yield of about 39.2% with respect to fluorescein. When compared to the pristine $CsPbBr_3$ QD colloidal solution a slight red shift from 518 nm to 519 nm was observed which could be attributed to the change in crystal size of $CsPbBr_3$ PeQDs while growing inside the MOF matrix. The wavelength of absorption onset of both the bare and MOF protected PeQDs matches well with the luminescence emission peak wavelength (Table 2.2).

The color of the PeQD@MOF composite can be easily adjusted by controlling the halide composition. The composite emits bright blue light under UV illumination of 365 nm when Br is partially exchanged with Cl. Both the composite exhibit dual emission peak. The emission maxima shifted to a lower wavelength with the addition of chloride content (Figure 2.11b), mainly due to the increased band gap energies of PeQDs with lighter halides ($I^- < Br^- < Cl^-$) [43]. With a further increase in chloride content, the emission maxima blue shifted to 430 nm (Figure 2.11c). Further, the FWHM value of the mixed halide composite increases indicating its less ordered halide arrangement in the crystal lattices of perovskite which is likely due to the difference in ionic radius of Br^- and Cl^-. However, the actual reason for broad emission FWHM is still unknown.
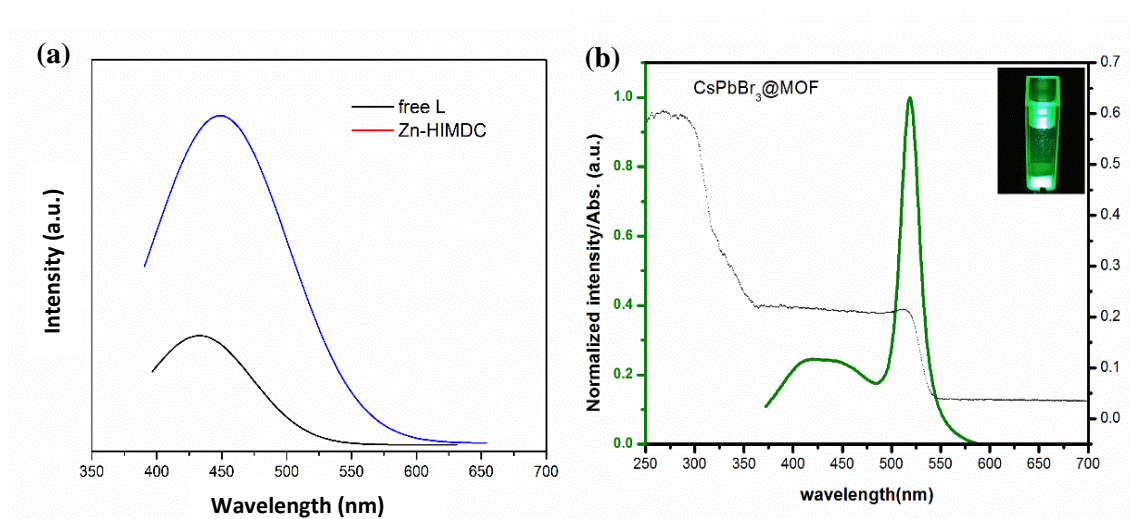

Figure 2.10: Photoluminescence spectrum of free linker (black) and the MOF (blue) (a), emission and absorption spectrum of $CsPbBr_3$@MOF composite (b).
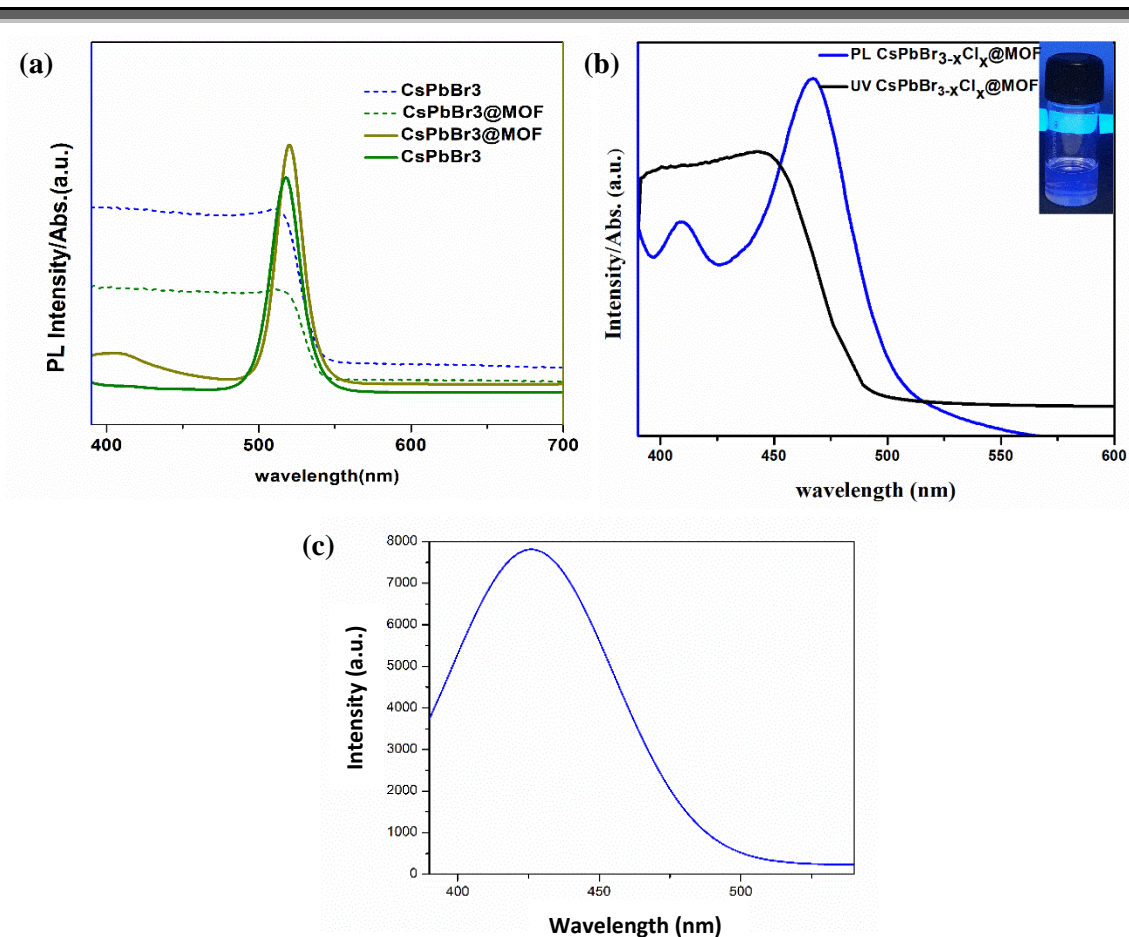
Figure 2.11: Comparison of PL and abs. spectra of $CsPbBr_3$ QD (LARP) and $CsPbBr_3$@MOF (a), abs. and PL spectrum of $CsPbBr_{3-x}Cl_x$@MOF composite (b), (c).

Table 2.2. Summary of photo physical properties of synthesized perovskites.

Samples	λ_{abs} (nm)	λ_{em} (nm)	FWHM (nm)	Band gap (eV)	PLQY (%)
CsPbBr₃	512	518	23.4	2.40	25
CsPbBr₃@MOF	513	519	20.5	2.39	39.2
CsPbBrₓCl₃₋ₓ@MOF	455	467	34.8	2.65	28

The time-resolved PL decay of $CsPbBr_3$@MOF can be illustrated to determine the lifetime of carriers. The decay measurements were performed at the emission wavelength of 518 nm and 410 nm under an excitation wavelength of 380 nm for $CsPbBr_3$@MOF and $CsPbBr_{3-x}Cl_x$@MOF respectively as shown in Figure 2.12a and Figure 2.12b. All the

curves were well fitted by the tri-exponential function as mentioned in the below equation (2.2).

$$Y = A_1 \exp(-x/\tau_1) + A_2 \exp(-x/\tau_2) + A_3 \exp(-x/\tau_3) \qquad (2.2)$$

Where τ_1, τ_2, and τ_3 are the exponential elements representing fast and slow lifetime decay parameters and A_1, A_2, and A_3 are constant termed as pre-exponential factors. The τ_{avg} denotes the average lifetime which can be calculated using the following equation.

$$\tau_{avg} = \frac{\Sigma A_i \tau_i 2}{\Sigma A_i \tau_i} \qquad (2.3)$$

The CsPbBr$_3$@MOF composite has longer average recombination lifetime (32.04 ns), as compared to bare CsPbBr$_3$ (τ_{avg}= 26.42 ns). Due to the presence of lighter halide (Cl) and smaller size, CsPbBr$_{3-x}$Cl$_x$@MOF (τ_{avg}= 2.18 ns) exhibits faster decay dynamics than green emissive CsPbBr$_3$@MOF [23,34]. The enhanced lifetime of MOF protected PeQDs than pristine CsPbBr$_3$ could be a result of surface passivation by the MOF that might reduce the surface trap states of CsPbX$_3$ PeQDs. It further restricts the non-radiative recombination pathway [35]. Table 2.3 describes the TRPL results of the synthesized products.

The broad blue emission of Zn-HIMDC MOF extends up to 600 nm. Thus, the absorption spectrum of CsPbBr$_3$ overlapped with the emission spectrum of MOF (Figure 2.13a), suggesting energy transfer from the donor host framework to the CsPbBr$_3$. The TRPL decay dynamics presented in Figure 2.13b further confirmed this assumption. Pure MOF in absence of CsPbBr$_3$ shows slower decay dynamics than the MOF in presence of CsPbBr$_3$. The MOF exhibited an average lifetime of 3.16 ns when TRPL was observed at an emission wavelength of 410 nm under excitation at 375 nm. The lifetime of blue emission of CsPbBr$_3$@MOF was reduced to 1.15 ns which shows the existence of energy transfer in CsPbBr$_3$@MOF.

Table 2.3. Summary of TRPL decay measurements

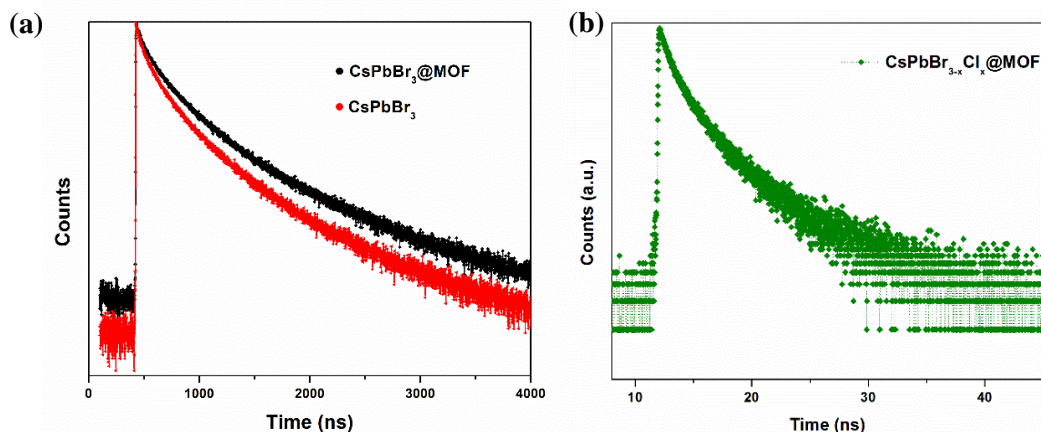| Sample	τ_1 (ns)	τ_2 (ns)	τ_3 (ns)	τ_{avg} (ns)	χ^2 (reduced chi square)
CsPbBr$_3$@MOF	10.67	21.36	42.73	32.04	1.09
CsPbBr$_3$	8.80	17.61	35.23	26.42	1.05
CsPbBr$_{3-x}$Cl$_x$@MOF	0.234	1.15	3.497	2.18	1.037
Zn-HIMDC MOF	0.297	1.416	4.283	3.16	1.024

Figure 2.12: TRPL decay dynamics of CsPbBr$_3$@MOF (black) and CsPbBr$_3$ QD (red) (a), CsPbBr$_{3-x}$Cl$_x$@MOF (b).
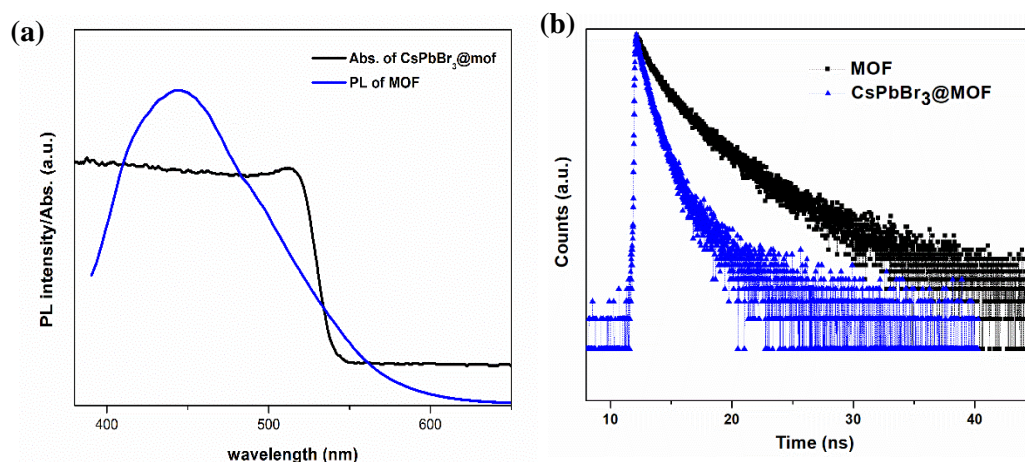

Figure 2.13: Overlapping of abs. spectra of CsPbBr$_3$@MOF and emission spectra of MOF (a), TRPL decays for MOF and CsPbBr$_3$@MOF in the blue region (b).

Using the equation (3), energy transfer efficiency (η) was found to be 63%.

$$\eta = 1 - (\int PL_{DA}(E)\ dE\ /\int PL_D\ (E)\ dE) = 1 - (\tau_{DA}/\tau_D) \tag{2.4}$$

Here, τ_D and τ_{DA} denote the average lifetime of donor MOF in the absence and presence of acceptor CsPbBr$_3$ QD respectively [44].

2.3.8. Stability test of CsPbBr$_3$@MOF

The photoluminescence stability study of CsPbBr$_3$@MOF composite was performed in various condition. We investigated the thermal stability, UV photo stability, moisture stability, and different solvent stability of the composite. Temperature dependence of the emission behavior of CsPbBr$_3$@MOF was examined within the range of 25°C to 160°C

under the excitation wavelength of 365 nm. The results presented in Figure 2.14a show that the PL intensity of $CsPbBr_3$@MOF gradually diminished with increasing the temperature. The $CsPbBr_3$@MOF composite preserves 67.9% of its original PL intensity at 85°C which indicates the better thermal stability of the resulting composite than the bare $CsPbBr_3$ PeQD with only 18% retention in PL intensity (Figure 2.14b). The $CsPbBr_3$@MOF can still emit green light beyond the temperature of 100°C whereas $CsPbBr_3$ QD emission almost disappeared at the same temperature.
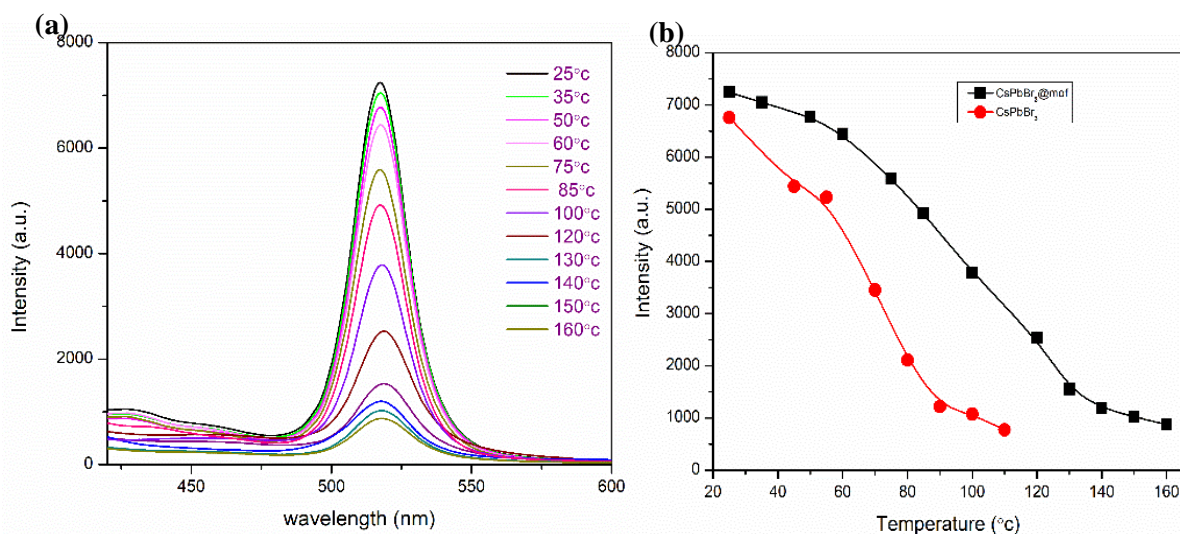

Figure 2.14: PL responses of $CsPbBr_3$@MOF with temperature (a), variation in intensity of $CsPbBr_3$@MOF and bare CsPbBr3 as a function of temperature (b).

UV photo-stability test of the $CsPbBr_3$@MOF composite was performed by exposing it to the 365 nm UV light in an ambient environment for 80 h and the PL intensity was checked at different intervals of exposure time. The $CsPbBr_3$@MOF composite retains 74.8% of its initial PL intensity when exposed to UV light (Figure 2.15a). Also, the composite displays excellent moisture stability. It preserves an initial PL intensity of 63.66% after 60 days of storage at room temperature in a humid environment (~ 60% humidity) (Figure 2.15b). Furthermore, to check the anion exchange property, $CsPbBr_3$@MOF and $CsPbBr_{3-x}Cl_x$@MOF composites dispersion in toluene were mixed. The PL spectrum of the mixture dispersion solution (Figure 2.15c) shows no peak shifting which indicates no anion exchange between the two. The MOF can prevent the ion exchange between the two perovskites.
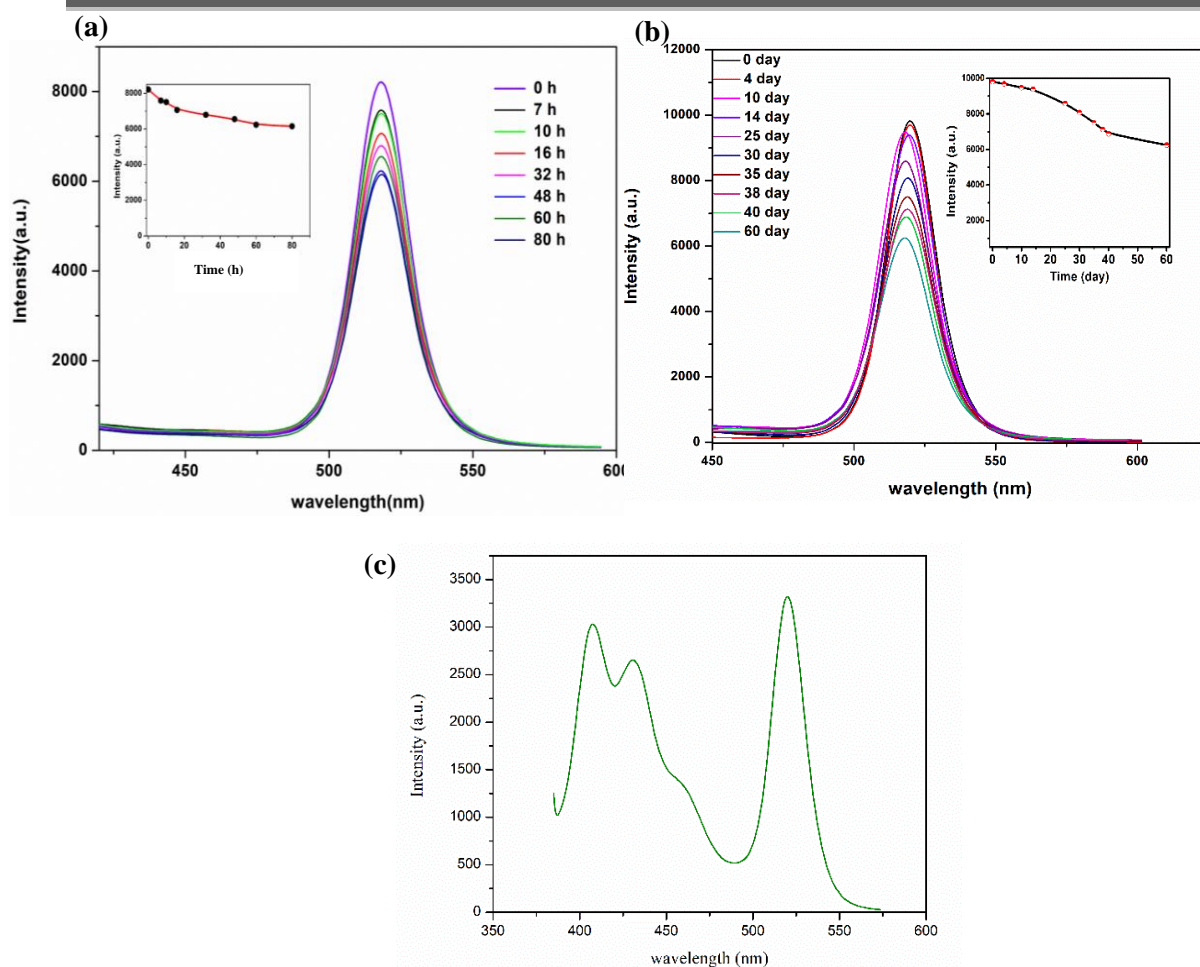
Figure 2.15: Storage test and UV Photo-stability test of CsPbBr$_3$@MOF composite (a, b), inset: Intensity vs. time plot, PL spectrum of mixture of CsPbBr$_3$@MOF and CsPbBr$_{3-x}$Cl$_x$@MOF dispersion (c).

The use of PeQDs is limited exclusively to non-polar solvents, making them unsuitable for a variety of practical applications. However, the above stated limitation is eradicated when the PeQDs are engulfed inside the pores of MOF. We have checked the solvent stability of the composite after immersing the CsPbBr$_3$@MOF powder in different polar solvents [water, methanol, ethanol, butanol, isopropanol (IPA), N,N-dimethylformamide (DMF), dimethyl sulfoxide (DMSO), ethyl acetate (EtOAc), 1-Methyl-2-Pyrrolidone (NMP), acetonitrile (ACN), etc.] for a few days. We investigated the emission spectrum of all the samples. Highly intense emission of the composite is shown to exist up to 5 days of immersion with no notable change in intensity. After immersion of the composite into water for 5 days, 24.8% of its initial PL intensity was retained. Table 2.4 illustrates the retained percentage of PL intensity in various solvents. Although emission intensity of the CsPbBr$_3$@MOF diminished in water in comparison to other solvents, it still emits green

light in water whereas in the case of bare $CsPbBr_3$ PeQD no emission was detected in water. The findings indicate the stability of the composite in polar solvents (Figure 2.16a). The impact of residual solvents on the sample luminescence reflects a little variation in intensity. Figure 2.16b clearly shows the rapid quenching of the PL intensity of $CsPbBr_3$ QD synthesized by the LARP method after immersing it in methanol. A noticeable red shift of 7 nm in the PL peak of $CsPbBr_3$ QD is observed from 518 nm to 525 nm on being dispersed in a polar solvent, indicating the particle aggregation effect of PeQDs due to the destruction of unstable surface ligands in polar solvents. However, no such situation arises for the $CsPbBr_3$@MOF composite, ensuring that the selected MOF in this work provides strong interaction of the PeQDs with the MOF surface that can safeguard the core of PeQDs by acting as a protective shell. Moreover, integrating $CsPBr_3$ PeQDs into the pores of MOF crystals could also restrict the aggregation of PeQDs by separating them from adjacent ones, therefore enhancing the stability considerably in contrast to $CsPbX_3$ PeQDs.
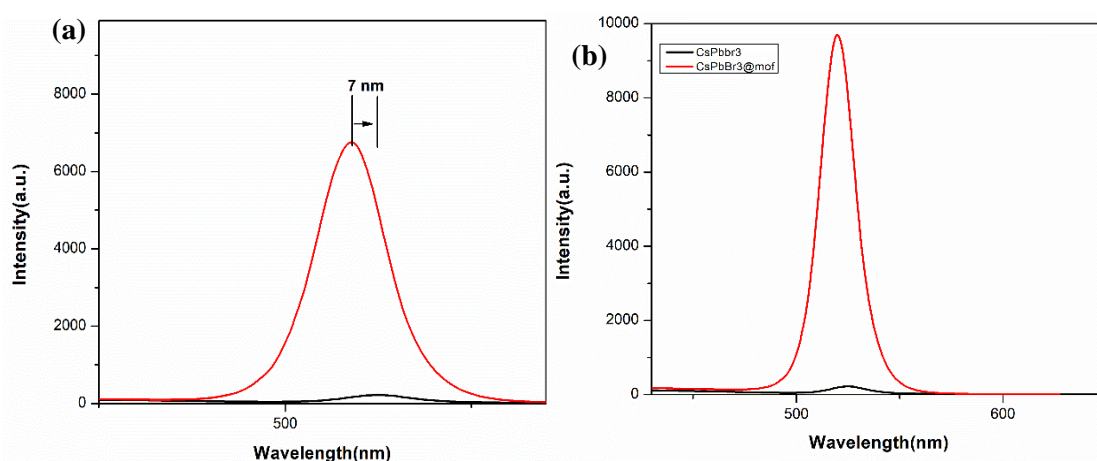

Figure 2.16: Comparison of PL intensity of $CsPbBr_3$@MOF composite and bare $CsPbBr_3$ PeQD in a polar solvent (a), PL peak shifting of bare $CsPbBr_3$ PeQD in a polar solvent (b).

We have further studied the photoluminescence response of $CsPbX_3$@MOF composite with different excitation wavelengths ranging from 280 to 470 nm (Figure 2.18). At 280 nm excitation, one less intense broad blue emission peak is observed which may be attributed to the intra ligand $\pi \rightarrow \pi^*$ transition of the MOF matrix. At this excitation, the composite scarcely gives green emission. As the excitation wavelength changes in a positive direction from 280-470 nm, the rate of green emission of $CsPbX_3$@MOF increases along with diminishing blue emission.
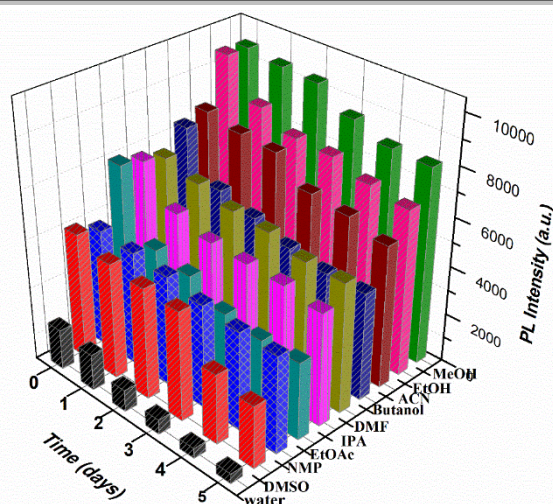
Figure 2.17 Emission of CsPbBr$_3$@MOF composite dispersed in different solvents.

Table 2.4. Chemical stability in various solvents

Percentage retained PL intensity					
Solvent	Day 1	Day 2	Day 3	Day 4	Day 5
Methanol	97.76	96.87	88.57	83.29	82.77
Ethanol	84.39	77.96	77.17	72.60	69.80
Butanol	74.38	68.58	62	58.60	58.49
Isopropanol	79.36	72.70	71.50	70.60	66.80
DMF	94.33	88.20	86.40	80.27	79.77
DMSO	91.55	88.06	86.47	55.11	49.14
Ethyl acetate	61.78	57.82	47.53	44.51	44.32
Acetonitrile	96.21	95	82.50	80.17	74.68
NMP	96.50	93.05	86.57	82.15	81.06
Water	89.32	74.40	72.70	53.54	24.86

It exhibits the highest PLE (photoluminescence emission) peak intensity at 360 nm excitation. With further increase in excitation wavelength up to 420 nm results in a less intense peak at 519 nm compared to excitation at 360 nm. These results are supported by excitation spectra of the CsPbBr$_3$@MOF at 519 nm emission (Figure 2.18b). It is noteworthy that there is no wavelength shift of green emission with different excitation wavelengths.
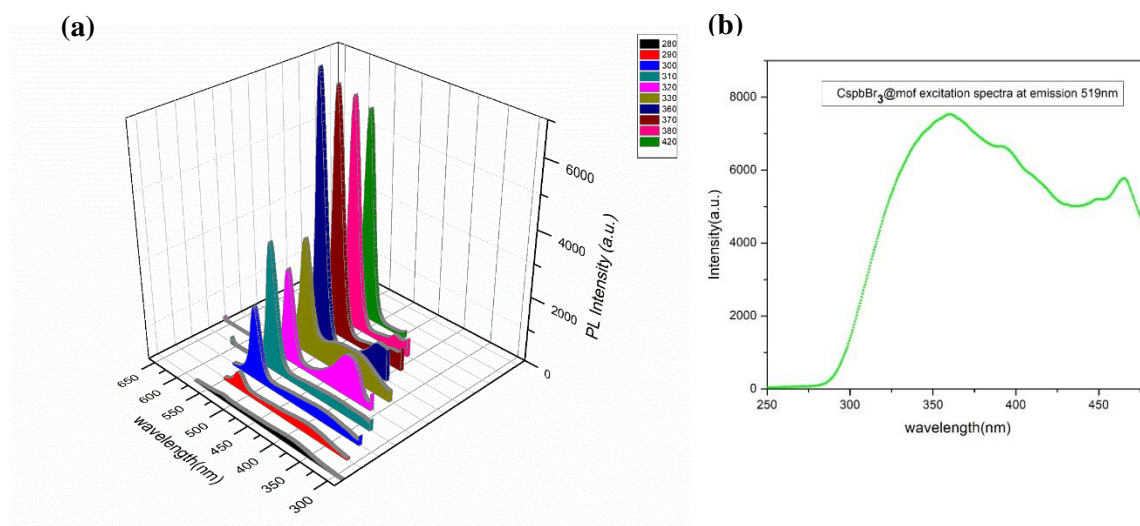

Figure 2.18: PL response with different excitation wavelength (a), Excitation spectra of CsPbBr$_3$@MOF composite at 519 nm emission wavelength (b).

2.3.9. Detection of metal ions by using CsPbBr$_3$@MOF

In comparison to bare CsPbBr$_3$ PeQDs, the CsPbBr$_3$@MOF nano hybrid exhibits superior stability, and its strong emission allows for high sensitivity for metal ion detection. The PL emission centered at 519 nm decreased when copper ion concentration increased from 5 to 1750 nM and can be clearly visible under UV light with naked eyes (Figure 2.19a). The excitation spectra of the composite at $\lambda_{emi} = 519$ nm was also depicted in Figure 2.19d, was quenched when Cu^{2+} was added into it. There was negligible influence of dilution on quenching, therefore we can say that solvent did not interfere with the sensitive quenching by metal ions. Stern-Volmer equation (4) was applied to analyze the quenching behavior of the CsPbBr$_3$@MOF emission at 519 nm using 365 nm excitation wavelength.

$$F_o/F = 1 + K_{SV}[C] \qquad\qquad (2.5)$$

Here F_o and F represent the PL emission intensities of perovskite QD before and after the addition of the analyte respectively, [C] is the molar concentration of Cu^{2+} and K_{SV} is the

Stern – Volmer quenching constant. A good linear relationship was obtained when relative PL intensities were plotted against concentrations of Cu^{2+} (Figure 2.19b) within the range of 5-1800 nM. The calibration plot well fitted to the equation, Y = 1.38743 + .00433 X, with correlation coefficient (R^2) value of 0.99433. The quenching constant (K_{sv}) value was found to be $4.33 \times 10^6 \, M^{-1}$. The theoretical limit of detection (LOD) was determined based on the standard deviation (σ) of the blank signal and the slope of the fitted line (S). Using the relation $3\sigma/S$, the LOD was found to be as low as 63 nM.

Moreover, we have studied the sensing behavior of pristine MOF with Cu^{2+} ion (Figure 2.20). In comparison to the $CsPbBr_3$@MOF composite, the parent MOF did not show effective quenching of Cu^{2+}. With the increase in the concentration of Cu^{2+} from 6.25 to 130 μM, the PL intensity of MOF quenched a little. The K_{sv} value for MOF is calculated to be $3.11 \times 10^3 \, M^{-1}$ which is much lower than the K_{sv} value of the hybrid perovskite-MOF composite. It signifies a weak quenching effect of pristine MOF.

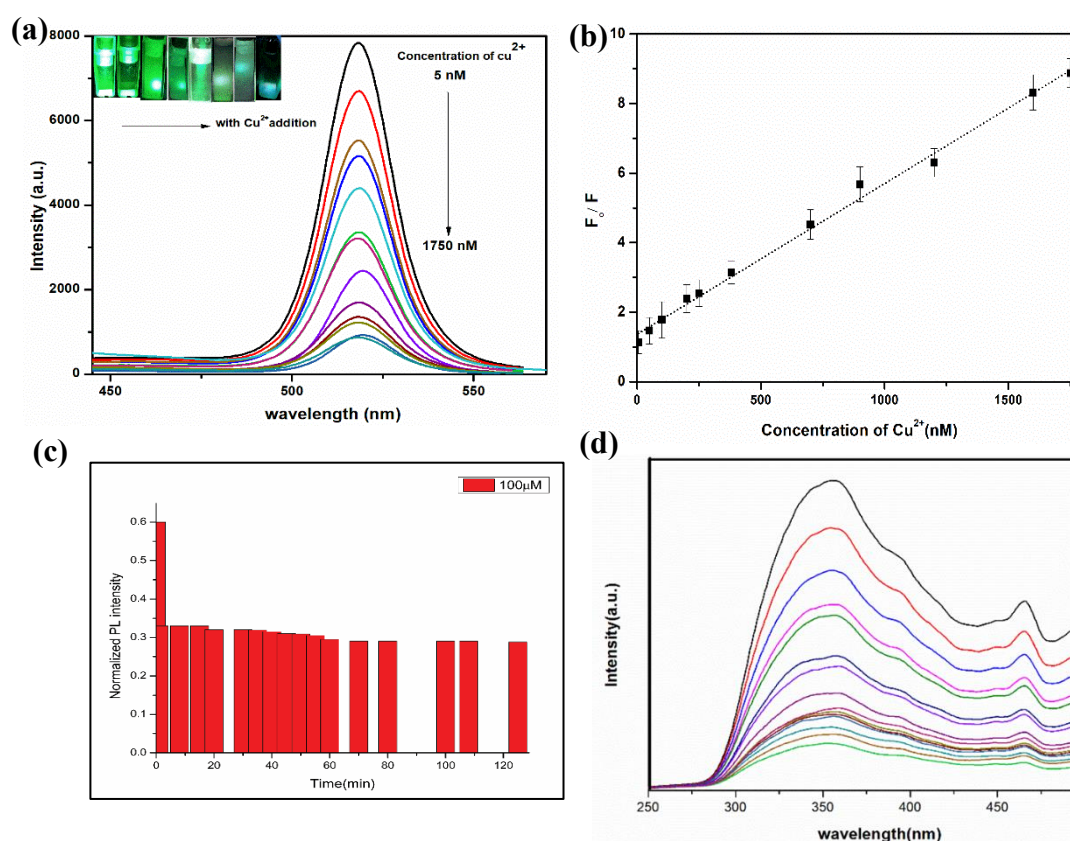**Figure 2.19:** Emission spectra of $CsPbBr_3$@MOF with the increasing concentration of Cu^{2+} metal ion (a), Stern-Volmer calibration plot (b), a plot of Pl intensity variation of the QD probe with an incubation time of 2h (c), Excitation spectrum at 519 nm emission with various concentration of copper ion (d).

The sensitivity of detection increases when the perovskite quantum dot is incorporated into the MOF matrix. Table 2.5 compares our results to other literature using MOF or MOF-based composite for Cu^{2+} detection studies. Our composite outperforms some of the literature.
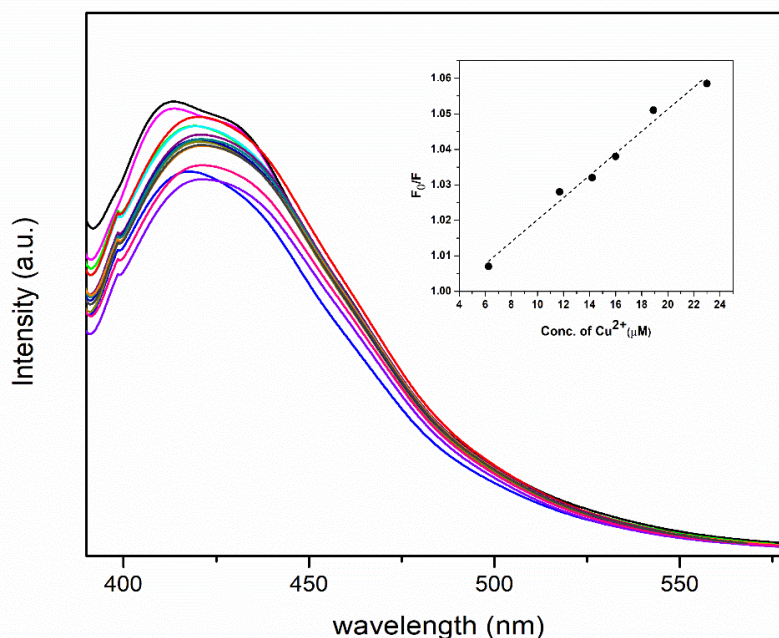

Figure 2.20: PL response of pristine MOF with various concentration of Cu^{2+} ion, inset: Stern – Volmer calibration plot of MOF for Cu^{2+} ion.

2.3.10. Selectivity study

To evaluate the selectivity of $CsPbBr_3$@MOF towards Cu^{2+} detection PL quenching was studied using various metal ions at the same concentration. The quenching efficiency of Cu^{2+} was the highest, showing a very good selectivity compared to other metal ions (Figure 2.21a). To further evaluate the practical applicability of the probe, an anti-interference test was performed by mixing Cu^{2+} with other metal ion solutions and PL quenching of the mixture solution was checked (Figure 2.21b). A slight change in quenching efficiency of Cu^{2+} was noticed which confirms the feasibility of this method for the determination of Cu^{2+}. The quenching process occurred so fast that the PL intensity decreased within one min and after that, no change in intensity was observed indicating the excellent stability of the system. Figure 2.19c presents the plot of PL intensity of $CsPbBr_3$@MOF in presence of a certain amount of Cu^{2+} for an incubation period of 2 h. This result confirms the reaction time independent sensing ability of the system for Cu^{2+} detection.

Table 2.5 Comparison of different MOF or MOF based composite material as a florescent probe for Cu^{2+} ion detection.

| Material	Performance/LOD	Performance range	Ref
Tb^{3+}-functionalized UiO-66	LOD = 0.23 μM $K_{sv} = 4.12 \times 10^4 \, M^{-1}$	0–200 μM	[45]
MOF-5-NH$_2$	LOD = 0.057 μM $K_{sv} = 2.68 \times 10^4 \, M^{-1}$	1 −10 μM	[46]
MOF-525	LOD = 67 nM, $K_{sv} = 4.5 \times 10^5 \, M^{-1}$	0–20 μM	[47]
BPEI-CQDs/ZIF-8	LOD = 80 pM	2 − 1000 nM	[48]
MIL-53-L	LOD = 10 μM $K_{sv} = 6.15 \times 10^3 \, M^{-1}$	0–500 μM	[49]
PCN-222-Pd(II)	LOD=50 nM $K_{sv} = N/A$	N/ A	[50]
MOF-525	LOD = 0.22 nM $K_{sv} = 2.56 \times 10^7 \, M^{-1}$	1.0–250 nM	[51]
Nd-MOF	LOD = 24.95 μM	0 to 10^{-3} M	[52]
CH$_3$NH$_3$PbBr$_3$@MOF-5	LOD= N/ A $K_{sv} = 2 \times 10^2 \, M^{-1}$	200 to 2000 μM	[32]
Eu-MOF	LOD = 10 μM $K_{sv} = 1.163 \times 10^3 \, M^{-1}$	N/ A	[53]
CsPbBr$_3$@Zn-HIMDC	LOD = 63 nM $K_{sv} = 4.33 \times 10^6 \, M^{-1}$	5-1750 nM	This work
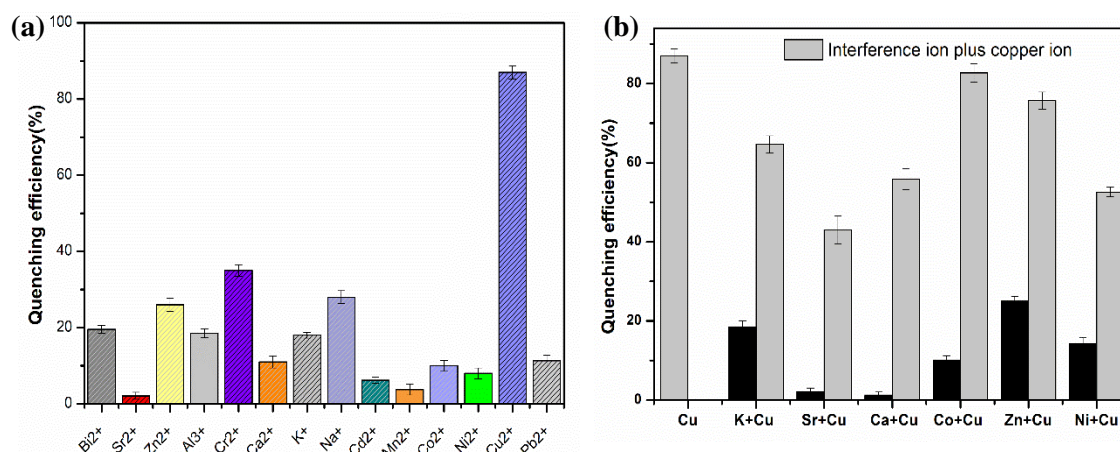
Figure 2.21: Quenching efficiency of various metal ions (a), PL quenching of the probe when Cu^{2+} was mixed with another metal ion (b).

2.3.11. Quenching mechanism

Photoluminescence quenching phenomenon can occur in a variety of ways, including i) Forster resonant energy transfer (FRET) ii) Inner filter effect (IFE) iii) charge transfer process iv) ion exchange phenomenon (static quenching), and so forth [54]. There is no significant overlap observed between the absorbance spectrum of copper ion, the emission spectrum and the excitation of the composite (Figure 2.22) which excludes the possibility of the FRET and IFE mechanism as for FRET to occur spectral overlap between the emission spectrum of the fluorophore and the absorption spectrum of analytes should occur. Also, no shift and change in the excitation and emission spectra were noticed after the addition of the Cu^{2+} into the system suggesting that the crystal size or conformation of PeQDs remains the same, ruling out the static quenching process between the quencher and fluorescent molecule which results in the formation of a ground state complex.

All these findings indicate that there might be a possibility of adsorption of Cu^{2+} on the surface of the probe. EDX analysis of the sensing system was carried out to investigate the existence of the Cu element on the surface of the $CsPbBr_3$@MOF composite. Figure 2.23a shows the appearance of the Cu signal along with the component element from MOF and $CsPbBr_3$ perovskite of the composite in the EDX spectrum. The X-ray photoelectron spectrometry (XPS) analysis was performed before and after the quenching experiment with Cu^{2+} to confirm the assumption. The XPS survey spectrum of $CsPbBr_3$@MOF shows no significant peak shifting after the introduction of Cu in the sensing probe (Figure 2.23b).
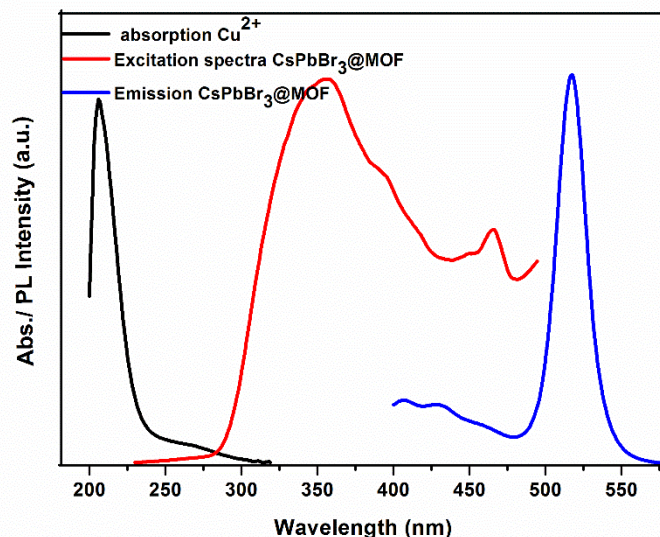
Figure 2.22: UV–vis absorption spectra of Cu^{2+} (black), excitation (Red), and emission spectra (blue) of $CsPbBr_3$@MOF.

Further to know the valency of Cu on the surface of the composite, high resolution XPS spectrum of Cu 2p was analyzed. As shown in figure 2.23c, the strong peak at 934.5 eV assigned Cu $2p_{3/2}$ hybrid orbits which confirm the presence of Cu^{2+} in $CsPbBr_3$@MOF [55]. Thereafter, fluorescence decay dynamics were studied to examine the quenching kinetics of the composite. As illustrated in figure 2.23d the fluorescence lifetime of $CsPbBr_3$@MOF composite reduces as $[Cu^{2+}]$ increases, corresponding to the PL intensity quenching. The average lifetime significantly drops to 26 ns from 32.04 ns in presence of 120 nM Cu^{2+} ion. Faster exciton decay dynamics of the fluorophore in presence of the target analyte offer a clear illustration of the nonradiative recombination pathways. Metal ion will react to the excited state of $CsPbBr_3$@MOF through electron transfer leading to a dynamic quenching process of the sensing system (Scheme 2.1). All these outcomes refer to the adsorption of Cu^{2+} on the surface resulting in the formation of surface modified states for non-radiative recombination pathways. As a result of this electrons can transfer from the PeQDs to Cu^{2+} with a reduction in PL intensity [56].
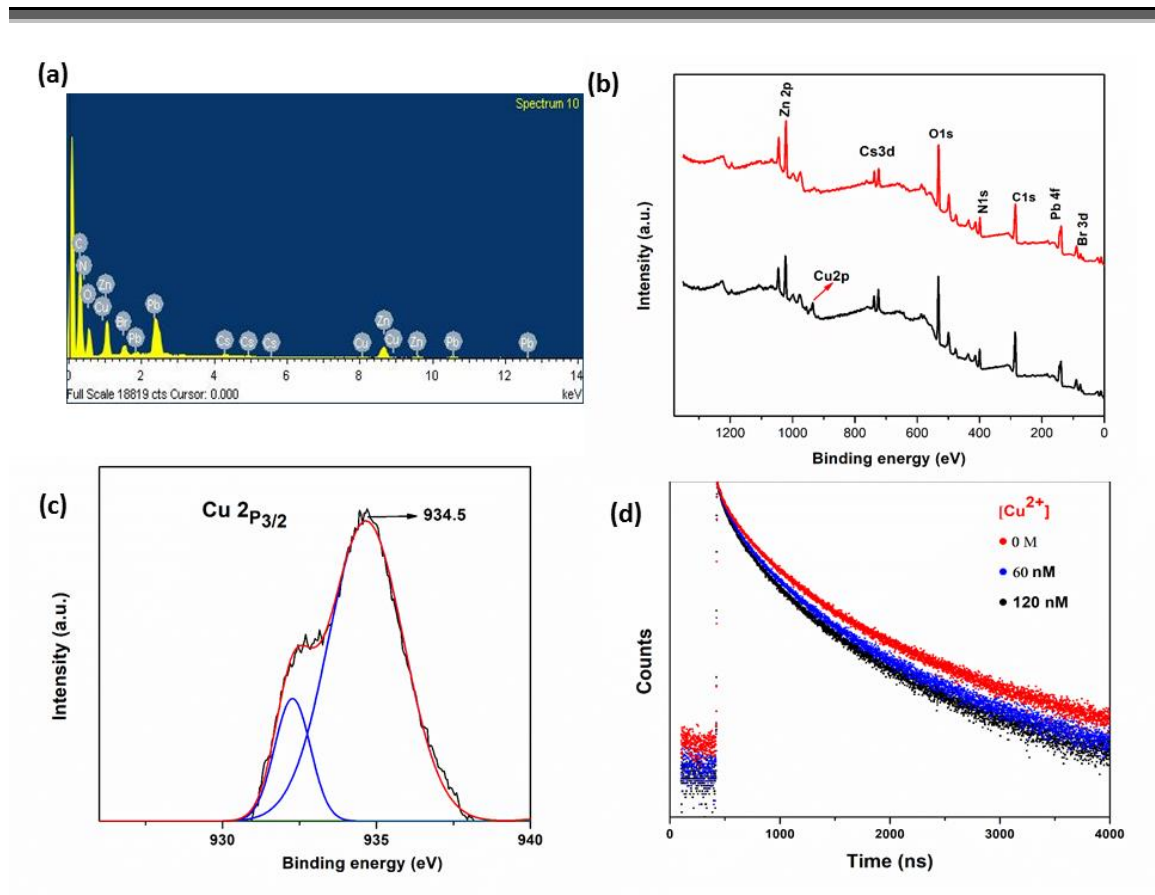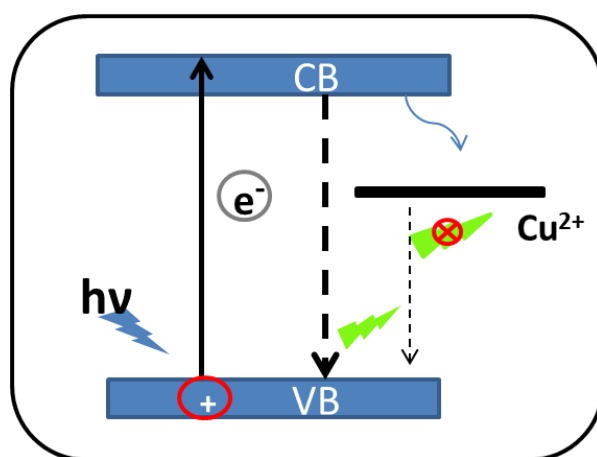
Figure 2.23: EDX spectrum of CsPbBr3@MOF after Cu sensing (a), XPS full survey spectra of CsPbBr3@MOF sensing probe with or without Cu^{2+} ion (b), High resolution XPS spectrum of Cu 2p (c), TRPL decay curve of $CsPbBr_3$@MOF with various concentrations of Cu^{2+} ion (d).

Scheme 2.1. Schematic illustration of the sensing mechanism.

2.3.12. Framework stability study after Cu^{2+} detection: To investigate the framework stability of the composite after the addition of Cu^{2+}, P-XRD and FTIR spectra of the sample were analyzed (Figure 2.24). No change in the characteristic diffraction peaks in XRD from the pristine MOF indicates that the framework is not damaged. Furthermore, the FTIR spectra also retain the original framework after Cu^{2+} addition indicating that the framework did not lose its structure throughout the process
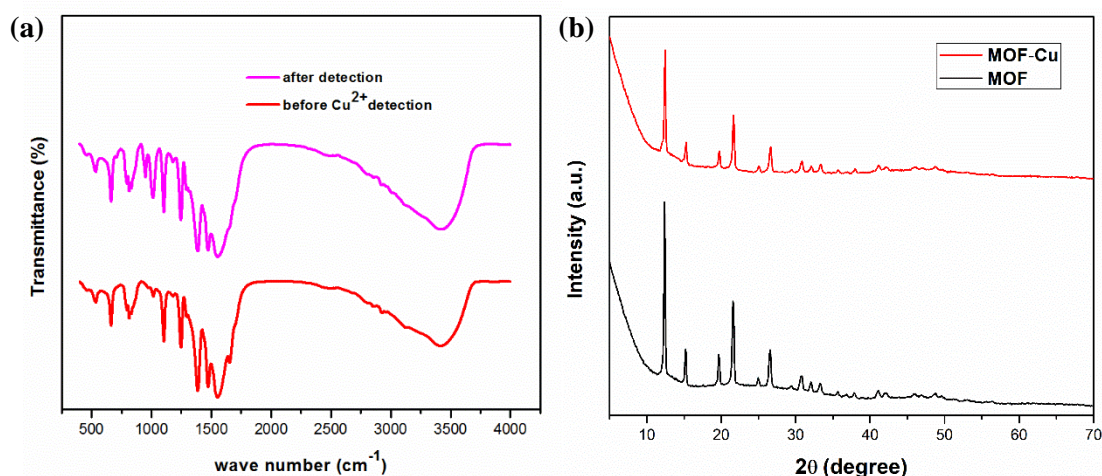

Figure 2.24: FTIR (a) PXRD (b) of Zn-HIMDC MOF before and after addition of Cu^{2+}.

2.4. Conclusion

✓ $CsPbX_3$@Zn-HIMDC (X = Br, Br/Cl) perovskite MOF hybrids were prepared via a facile surfactant free two step in-situ growth method by passivating $CsPbX_3$ with Zn based MOF. Successful formation of the composite was verified by FTIR, XRD, SEM, TEM, and XPS analysis.

✓ The $CsPbBr_3$@MOF composite shows narrow bright green emission at 519 nm with FWHM value of 20.5 nm, and utilizes energy transfer from the MOF.

✓ The composite shows enhanced stability against moisture, ultraviolet light, heat and polar solvents over bare $CsPbBr_3$ QD.

✓ The excellent PL properties instead of the harsh environment condition makes them an attractive candidate for fluorescence assays and is found to be very sensitive towards the detection of Cu^{2+} with a LOD value of 63 nM.

✓ The $CsPbBr_3$/MOF composite displays excellent quenching efficiency up to 89.9% for Cu metal ion in comparison with the other metal ions, which exhibit very low quenching efficiency.

✓ The integration of CsPbBr$_3$ to a chemically stable zeolitic imidazolate framework (ZIF-8) was covered in the next chapter (Chapter 3) in order to create a FL sensor that can identify organic contaminants (nitroaromatics and dye molecules).

2.5. References

[1]   Zhang, F., Zhong, H., Chen, C., Wu, X. G., Hu, X., Huang, H., Han, J., Zou, B., and Dong, Y. Brightly luminescent and color-tunable colloidal CH3NH3PbX3 (X= Br, I, Cl) quantum dots: potential alternatives for display technology. *ACS nano*, 9(4): 4533-4542, 2015.

[2]   Dutta, A., Pradhan, N. Phase-stable red-emitting CsPbI3 nanocrystals: successes and challenges, *ACS Energy Letters*, 4(3):709-19, 2019.

[3]   Worku, M., Tian, Y., Zhou, C., Lin, H., Chaaban, M., Xu, L. J., He, Q., Beery, D., Zhou, Y., Lin, X., and Su, Y. F. Hollow metal halide perovskite nanocrystals with efficient blue emissions, *Science Advances*, 6(17):5961, 2020.

[4]   Palazon, F., Di Stasio, F., Akkerman, Q. A., Krahne, R., Prato, M., and Manna, L. Polymer-free films of inorganic halide perovskite nanocrystals as UV-to-white color-conversion layers in LEDs. *Chemistry of Materials*, 28(9): 2902-2906, 2016.

[5]   Parida, B., Ryu, J., Yoon, S., Lee, S., Seo, Y., Cho, J. S., and Kang, D. W. Two-step growth of CsPbI 3− X Br X films employing dynamic CsBr treatment: Toward all-inorganic perovskite photovoltaics with enhanced stability. *Journal of Materials Chemistry A*, 7(31): 18488-18498, 2019.

[6]   Wang, Y., Dar, M. I., Ono, L. K., Zhang, T., Kan, M., Li, Y., Zhang, L., Wang, X., Yang, Y., and Gao, X. Thermodynamically stabilized β-CsPbI3–based perovskite solar cells with efficiencies> 18%. *Science*, 365(6453): 591-595, 2019.

[7]   Ramasamy, P., Lim, D.-H., Kim, B., Lee, S.-H., Lee, M.-S., and Lee, J. S. All-inorganic cesium lead halide perovskite nanocrystals for photodetector applications. *Chemical communications*, 52(10): 2067-2070, 2016.

[8]   Zhang, H., Wang, X., Liao, Q., Xu, Z., Li, H., Zheng, L., and Fu, H. Embedding perovskite nanocrystals into a polymer matrix for tunable luminescence probes in cell imaging. *Advanced Functional Materials*, 27(7): 1604382, 2017.

[9]   Kou, H., Pang, S., Yang, B., Wang, M., Ding, J., Zhang, Z., and Yang, X. A dual-emission ratiometric fluorescent nanoprobe based on silicon nanoparticles and carbon dots for efficient detection of Cu (ii). *CrystEngComm*, 23(13): 2599-2605, 2021.

[10] Liu, Y., Tang, X., Zhu, T., Deng, M., Ikechukwu, I. P., Huang, W., Yin, G., Bai, Y., Qu, D., and Huang, X. All-inorganic CsPbBr 3 perovskite quantum dots as a photoluminescent probe for ultrasensitive Cu 2+ detection. *Journal of Materials Chemistry C*, 6(17): 4793-4799, 2018.

[11] Cardenas-Morcoso, D., Gualdrón-Reyes, A. s. F., Ferreira Vitoreti, A. B., García-Tecedor, M., Yoon, S. J., Solis de la Fuente, M., Mora-Seró, I., and Gimenez, S. Photocatalytic and photoelectrochemical degradation of organic compounds with all-inorganic metal halide perovskite quantum dots. *The journal of physical chemistry letters*, 10(3): 630-636, 2019.

[12] Wang, K., Jin, Z., Liang, L., Bian, H., Bai, D., Wang, H., Zhang, J., Wang, Q., and Liu, S. All-inorganic cesium lead iodide perovskite solar cells with stabilized efficiency beyond 15%. *Nature communications*, 9(1): 4544, 2018.

[13] Li, B., Zhang, Y., Fu, L., Yu, T., Zhou, S., Zhang, L., and Yin, L. Surface passivation engineering strategy to fully-inorganic cubic CsPbI3 perovskites for high-performance solar cells. *Nature communications*, 9(1): 1076, 2018.

[14]   Protesescu, L., Yakunin, S., Bodnarchuk, M. I., Krieg, F., Caputo, R., Hendon, C. H., Yang, R. X., Walsh, A., and Kovalenko, M. V. Nanocrystals of cesium lead halide perovskites (CsPbX3, X= Cl, Br, and I): novel optoelectronic materials showing bright emission with wide color gamut. *Nano letters*, 15(6): 3692-3696, 2015.

[15] Bekenstein, Y., Koscher, B. A., Eaton, S. W., Yang, P., and Alivisatos, A. P. Highly luminescent colloidal nanoplates of perovskite cesium lead halide and their oriented assemblies. *Journal of the American Chemical Society*, 137(51), 16008-16011, 2015.

[16] Bera, S., Ghosh, D., Dutta, A., Bhattacharyya, S., Chakraborty, S., and Pradhan, N. Limiting heterovalent B-site doping in CsPbI3 nanocrystals: phase and optical stability. *ACS Energy Letters*, 4(6):1364-1369, 2019.

[17] Sun, J. Y., Rabouw, F. T., Yang, X. F., Huang, X. Y., Jing, X. P., Ye, S., and Zhang, Q. Y. Facile two-step synthesis of all-inorganic perovskite CsPbX3 (X= Cl,

Br, and I) zeolite-Y composite phosphors for potential backlight display application. *Advanced Functional Materials*, 27(45):1704371, 2017.

[18] Gong, Y., Shen, J., Zhu, Y., Yang, X., Zhang, L., and Li, C. Stretch induced photoluminescence enhanced perovskite quantum dot polymer composites. *Journal of Materials Chemistry C*, 8(4):1413-1420, 2020.

[19] Xin, Y., Zhao, H., and Zhang, J. Highly stable and luminescent perovskite–polymer composites from a convenient and universal strategy. *ACS applied materials & interfaces*, 10(5):4971-4980, 2018.

[20] Qian, C. X., Deng, Z. Y., Yang, K., Feng, J., Wang, M. Z., Yang, Z., Liu, S. F., and Feng, H. J. Interface engineering of CsPbBr3/TiO2 heterostructure with enhanced optoelectronic properties for all-inorganic perovskite solar cells. *Applied Physics Letters*, 112(9), 2018.

[21] Zhong, Q., Cao, M., Hu, H., Yang, D., Chen, M., Li, P., Wu, L., and Zhang, Q. One-pot synthesis of highly stable CsPbBr3@ SiO2 core–shell nanoparticles. *ACS nano*, 12(8): 8579-8587, 2018.

[22] Li, Z., Kong, L., Huang, S., and Li, L. Highly luminescent and ultrastable CsPbBr3 perovskite quantum dots incorporated into a silica/alumina monolith. *Angewandte Chemie*, 129(28):8246-8250, 2017.

[23] Wei, Y., Xiao, H., Xie, Z., Liang, S., Liang, S., Cai, X., Huang, S., Al Kheraif, A. A., Jang, H. S., and Cheng, Z. Highly luminescent lead halide perovskite quantum dots in hierarchical CaF2 matrices with enhanced stability as phosphors for white light-emitting diodes. *Advanced Optical Materials*, 6(11): 1701343, 2018.

[24] Li, Y., Dong, L., Patterson, R., Teh, Z. L., Hu, Y., Huang, S., and Chen, C. Stabilizing CsPbBr3 perovskite quantum dots on zirconium phosphate nanosheets through an ion exchange/surface adsorption strategy. *Chemical Engineering Journal*, 381, 122735, 2020.

[25] Chen, W., Zhuang, Y., Wang, L., Lv, Y., Liu, J., Zhou, T. L., and Xie, R. J. Color-tunable and high-efficiency dye-encapsulated metal–organic framework composites used for smart white-light-emitting diodes. *ACS applied materials & interfaces*, 10(22):18910-18917, 2018.

[26] Ye, S., Sun, J. Y., Han, Y. H., Zhou, Y. Y., and Zhang, Q. Y. Confining Mn2+-doped lead halide perovskite in zeolite-Y as ultrastable orange-red phosphor composites for white light-emitting diodes. *ACS applied materials & interfaces*, 10(29):24656-24664, 2018.

[27] Hou, J., Wang, Z., Chen, P., Chen, V., Cheetham, A. K., and Wang, L. Intermarriage of halide perovskites and metal-organic framework crystals. *Angewandte Chemie*, 132(44):19602-19617, 2020.

[28] Shen, K., Zhang, L., Chen, X., Liu, L., Zhang, D., Han, Y., Chen, J., Long, J., Luque, R., Li, Y. and Chen, B. Ordered macro-microporous metal-organic framework single crystals. *Science*, 359(6372):206-210, 2018.

[29] Dang, G. H., Vu, Y. T., Dong, Q. A., Le, D. T., Truong, T. and Phan, N. T. Quinoxaline synthesis via oxidative cyclization reaction using metal–organic framework Cu (BDC) as an efficient heterogeneous catalyst. *Applied Catalysis A: General*, 491:189-195, 2015.

[30] Chen, S. S., Han, S. S., Ma, C.B., Li, W. D. and Zhao, Y. A series of metal–organic frameworks: Syntheses, structures and luminescent detection, gas adsorption, magnetic properties. *Crystal Growth & Design*, 21(2):869-885, 2021.

[31] Wu, M. X. and Yang, Y. W. Metal–organic framework (MOF)-based drug/cargo delivery and cancer therapy. *Advanced Materials*, 29(23):1606134, 2017.

[32] Zhang, D., Xu, Y., Liu, Q. and Xia, Z. Encapsulation of CH3NH3PbBr3 perovskite quantum dots in MOF-5 microcrystals as a stable platform for temperature and aqueous heavy metal ion detection. *Inorganic chemistry*, 57(8):4613-4619, 2018.

[33] Zhang, D., Zhou, W., Liu, Q. and Xia, Z. CH3NH3PbBr3 perovskite nanocrystals encapsulated in lanthanide metal–organic frameworks as a photoluminescence converter for anti-counterfeiting. *ACS applied materials & interfaces*, 10(33):27875-27884, 2018.

[34] Rambabu, D., Bhattacharyya, S., Singh, T., ML, C. and Maji, T. K. Stabilization of MAPbBr3 perovskite quantum dots on perovskite MOFs by a one-step mechanochemical synthesis. *Inorganic chemistry*, 59(2):1436-1443, 2020.

[35] Ren, J., Li, T., Zhou, X., Dong, X., Shorokhov, A. V., Semenov, M. B., Krevchik, V. D. and Wang, Y. Encapsulating all-inorganic perovskite quantum dots into mesoporous metal organic frameworks with significantly enhanced stability for optoelectronic applications. *Chemical Engineering Journal*, 358:30-39, 2019.

[36] Zhang, D., Zhao, J., Liu, Q. and Xia, Z. Synthesis and luminescence properties of CsPbX3@ Uio-67 composites toward stable photoluminescence convertors. *Inorganic Chemistry*, 58(2):1690-1696, 2019.

[37] Ren, J., Zhou, X. and Wang, Y. Dual-emitting CsPbX3@ ZJU-28 (X= Cl, Br, I) composites with enhanced stability and unique optical properties for multifunctional applications. *Chemical Engineering Journal*, 391:123622, 2020.

[38] Fang, R. Q. and Zhang, X. M. Diversity of coordination architecture of metal 4, 5-dicarboxyimidazole. *Inorganic chemistry*, 45(12):4801-4810, 2006.

[39] Zhong, R. Q., Zou, R. Q. and Xu, Q. Microporous metal-organic framework zinc (II) imidazole-4, 5-dicarboxylate: Four-fold helical structure and strong fluorescent emission. *Microporous and mesoporous materials*, 102(1-3):122-127, 2007.

[40] Zhang, C., Wang, B., Li, W., Huang, S., Kong, L., Li, Z. and Li, L. Conversion of invisible metal-organic frameworks to luminescent perovskite nanocrystals for confidential information encryption and decryption. *Nature communications*, 8(1):1138, 2017.

[41] Williams, A. T. R., Winfield, S. A., and Miller, J. N. Relative fluorescence quantum yields using a computer-controlled luminescence spectrometer. *Analyst*, 108(1290), 1067-1071, 1983.

[42] Zhong, R. Q., Zou, R. Q., Du, M., Takeichi, N. and Xu, Q. Observation of helical water chains reversibly inlayed in magnesium imidazole-4, 5-dicarboxylate. *CrystEngComm*, 10(9):1175-1179, 2008.

[43] Cha, J. H., Noh, K., Yin, W., Lee, Y., Park, Y., Ahn, T. K., Mayoral, A., Kim, J., Jung, D. Y. and Terasaki, O. Formation and encapsulation of all-inorganic lead halide perovskites at room temperature in metal–organic frameworks. *The Journal of Physical Chemistry Letters*, 10(9):2270-2277, 2019.

[44] Shen, X., Sun, C., Bai, X., Zhang, X., Wang, Y., Wang, Y., Song, H. and Yu, W. W. Efficient and stable CsPb (Br/I) 3@ anthracene composites for white light-emitting devices. *ACS applied materials & interfaces*, 10(19):16768-16775, 2018.

[45] Peng, X. X., Bao, G. M., Zhong, Y. F., He, J. X., Zeng, L., and Yuan, H. Q. Highly selective detection of Cu2+ in aqueous media based on Tb3+-functionalized metal-organic framework. *Spectrochimica Acta Part A: Molecular and Biomolecular Spectroscopy*, 240:118621, 2020.

[46] An, X., Tan, Q., Pan, S., Liu, H., & Hu, X. A turn-on luminescence probe based on amino-functionalized metal-organic frameworks for the selective detections of Cu2+, Pb2+ and pyrophosphate. *Spectrochimica Acta Part A: Molecular and Biomolecular Spectroscopy*, 247:119073, 2021.

[47] Li, L., Shen, S., Lin, R., Bai, Y., and Liu, H. Rapid and specific luminescence sensing of Cu (II) ions with a porphyrinic metal–organic framework. *Chemical Communications*, 53(72):9986-9989, 2017.

[48] Lin, X., Gao, G., Zheng, L., Chi, Y., and Chen, G. Encapsulation of strongly fluorescent carbon quantum dots in metal–organic frameworks for enhancing chemical sensing. *Analytical chemistry*, 86(2):1223-1228, 2014.

[49] Liu, C., and Yan, B. A novel photofunctional hybrid material of pyrene functionalized metal-organic framework with conformation change for fluorescence sensing of Cu2+. *Sensors and Actuators B: Chemical*, 235:541-546, 2016.

[50] Chen, Y. Z., & Jiang, H. L. (2016). Porphyrinic metal–organic framework catalyzed heck-reaction: fluorescence "turn-on" sensing of Cu (II) ion. *Chemistry of Materials*, *28*(18):6698-6704.

[51] Cheng, C., Zhang, R., Wang, J., Zhang, Y., Wen, C., Tan, Y., and Yang, M. An ultrasensitive and selective fluorescent nanosensor based on porphyrinic metal–organic framework nanoparticles for Cu 2+ detection. *Analyst*, 145(3):797-804, 2020.

[52] Luo, J., Liu, B. S., Cao, C., and Wei, F. Neodymium (III) organic frameworks (Nd-MOF) as near infrared fluorescent probe for highly selectively sensing of Cu2+. *Inorganic Chemistry Communications*, 76:18-21, 2017.

[53] Zhang, L. N., Liu, A. L., Liu, Y. X., Shen, J. X., Du, C. X., and Hou, H. W. A luminescent europium metal–organic framework with free phenanthroline sites for highly selective and sensitive sensing of Cu2+ in aqueous solution. *Inorganic Chemistry Communications*, 56:137-140, 2015.

[54] Halali, V. V., Sanjayan, C. G., Suvina, V., Sakar, M., and Balakrishna, R. G. Perovskite nanomaterials as optical and electrochemical sensors. *Inorganic Chemistry Frontiers*, 7(14), 2702-2725, 2020.

[55] Xu, L., Yang, Y., Hu, Z. W., and Yu, S. H. Comparison study on the stability of copper nanowires and their oxidation kinetics in gas and liquid. *ACS nano*, 10(3):3823-3834, 2016.

[56] Ding, N., Zhou, D., Pan, G., Xu, W., Chen, X., Li, D., Zhang, X., Zhu, J., Ji, Y. and Song, H., Europium-doped lead-free Cs3Bi2Br9 perovskite quantum dots and ultrasensitive Cu2+ detection. *ACS Sustainable Chemistry & Engineering*, 7(9):8397-8404, 2019.